

Online Research @ Cardiff

This is an Open Access document downloaded from ORCA, Cardiff University's institutional repository: <https://orca.cardiff.ac.uk/id/eprint/120433/>

This is the author's version of a work that was submitted to / accepted for publication.

Citation for final published version:

Sedighi, Majid, Thomas, Hywel R. ORCID: <https://orcid.org/0000-0002-3951-0409> and Vardon, Philip J. 2018. Reactive transport of chemicals in compacted bentonite under nonisothermal water infiltration. Journal of Geotechnical and Geoenvironmental Engineering 144 (10) , 04018075. 10.1061/(ASCE)GT.1943-5606.0001955 file

Publishers page: [http://dx.doi.org/10.1061/\(ASCE\)GT.1943-5606.00019...](http://dx.doi.org/10.1061/(ASCE)GT.1943-5606.00019...)
<[http://dx.doi.org/10.1061/\(ASCE\)GT.1943-5606.0001955](http://dx.doi.org/10.1061/(ASCE)GT.1943-5606.0001955)>

Please note:

Changes made as a result of publishing processes such as copy-editing, formatting and page numbers may not be reflected in this version. For the definitive version of this publication, please refer to the published source. You are advised to consult the publisher's version if you wish to cite this paper.

This version is being made available in accordance with publisher policies.

See

<http://orca.cf.ac.uk/policies.html> for usage policies. Copyright and moral rights for publications made available in ORCA are retained by the copyright holders.



Reactive transport of chemicals in compacted bentonite under non-isothermal water infiltration

Majid Sedighi^{1*}, Hywel R. Thomas², Philip J. Vardon^{3*}

Abstract

This paper presents an investigation of coupled thermal, hydraulic and chemical behaviour of compacted bentonite buffer under heating and hydration conditions of the geological disposal of high level nuclear waste. The study presented provides further insight into the evolution of hydro-geochemistry of the compacted bentonite and the clay microstructure effects through a numerical modelling development of the reactive transport of multicomponent chemicals. The application/validation case study is based on a series of laboratory tests on heating and hydration of compacted bentonite for a period of 0.5 to 7.6 years reported in the literature. The effects of microstructure evolution during hydration and dehydration on the transport phenomena are included via a new approach that links the geochemistry of clay hydration/dehydration with the transport properties. The analysis results related to the moisture flow and chloride transport demonstrate close correlation with the experimental results by the inclusion of the effects of microstructure evolution in the transport phenomena. The results of numerical analysis of reactive transport of chemicals highlight the importance of accessory minerals present in bentonite on the distribution of some anionic species. The behaviour of major cationic species is shown to be mainly governed by the transport processes. Further insights into the processes associated with the elevated temperature effects of clay buffer are presented and discussed that are captured from the modelling results of clay-water-chemical system under coupled thermal and hydraulic conditions.

Keywords

Compacted bentonite, reactive transport, coupled behaviour, hydro-geochemistry, clay microstructure.

¹Lecturer, School of Mechanical, Aerospace and Civil Engineering, The University of Manchester, Manchester, M13 9PL, UK (corresponding author) E-mail: Majid.Sedighi@manchester.ac.uk. ² Professor, Geoenvironmental Research Centre, School of Engineering, Cardiff University, Cardiff CF24 3AA, UK E-mail: ThomasHR@cardiff.ac.uk. ³Associate Professor, Section of Geo-Engineering, Delft University of Technology, 2600 GA, Delft, P.O. Box 5048, the Netherlands. E-mail: P.J.Vardon@tudelft.nl. *Formerly, Research Fellow, Geoenvironmental Research Centre, Cardiff University, Cardiff, CF24 3AA, UK.

1. Introduction

The application of swelling clays in a compacted form is envisaged as a key component of the Engineered Barrier System (EBS) in geological concepts for the disposal of high level radioactive waste (HLW). It has been shown that the engineering behaviour of compacted swelling clays is strongly coupled with the hydro-geochemical processes that can occur in the clay-water-chemical system (e.g. Push and Yong, 2006; Steefel et al., 2010). Under variable thermal, hydraulic and chemical environment of the geological repository, geochemical interactions between the ionic species, clay and accessory minerals can induce considerable changes on the physical, chemical and mechanical behaviour of the clay buffer. An in-depth understanding of the multiphase, multicomponent and interacting hydro-geochemical system of the clay-water and its evolution under chemically-coupled processes is therefore important for the performance assessment of the compacted clay buffer. The study presented here aims to provide further insight into the evolution of hydro-geochemistry of compacted bentonite through coupled modelling of thermal, hydraulic and chemical processes.

An evolutionary phase in the operational life of the clay buffer under the conditions of the HLW repository starts after the emplacement of the buffer in the depositional holes where the partially saturated compacted bentonite can be exposed to an elevated temperature at the boundary adjacent to the HLW canister (heating) and re-saturation at the interface with the host rock (hydration). Considerable attempts have been made over the last three decades or so to study the physical, chemical/geochemical and mechanical behaviour of compacted bentonite buffer under heating and hydration effects through experimental studies at different scales (e.g. Martín et al., 2000; ENRESA, 2000; Cuevas et al., 2002; Villar et al., 2008a) and numerical modelling investigations that have been tested against the results of laboratory, mock-up and in-situ heating and hydration tests (e.g. Guimarães et al., 2007; Cleall et al., 2007; Samper et al., 2008; Zheng and Samper, 2008; Villar et al. 2008b; Steefel et al. 2010). There are also numerical modelling studies on the long-term behaviour of compacted bentonite as part of the engineered barrier systems (e.g. Arcos et al., 2008; Yang et al., 2008).

The coupled modelling study presented in this paper is based on a notable series of laboratory-scale heating and hydration tests on compacted FEBEX bentonite reported in the literature (Villar et al., 2007; Villar et al., 2008a; Villar et al., 2008b; Fernández and Villar, 2010). The series of heating and hydration experiments described above have been carried out on cylindrical samples of FEBEX bentonite, compacted at dry density around 1650 kg/m^3 and tested for periods 0.5, 1, 2, and 7.6 years. Figure 1 presents a schematic of the heating and hydration experiments whose results have been used. The results of geochemical *post-mortem* hydro-geochemical analysis of the heating and hydration tests have been reported by Villar et al. (2008b) and Fernández and Villar (2010) that provide extensive data and important insight into the evolution of hydro-geochemistry of the compacted bentonite at the end of experiments. However, data presented and knowledge gained is mainly based on the analysis after completion of the tests (i.e. 0.5, 1, 2, and 7.6 years) in which the conditions of the tests were different from the thermal and hydraulic conditions inside the sample (in-situ conditions) during the heating and hydrations. Specifically, the concentration of ionic species have been measured in the laboratory at a solid to liquid ratio of 1:4 and at 20°C that are different from the in situ conditions at the end of the tests associated with each slice of the sample.

The numerical modelling and investigation presented aims to i) provide a more comprehensive understanding of the transient hydro-geochemical processes during the heating and hydration tests on compacted bentonite (hereafter: transient analysis), ii) obtain a better understanding of temporal evolution of the soil-water-chemical system that is not directly possible to obtain from the experimental results and iii) examine the validity of the numerical model developed and applied against an experimental dataset at the end of the transient analyses considering similar temperature and water content conditions applied in the post-mortem experiments (hereafter: post-mortem analysis).

An important aspect in the prediction of behaviour of compacted clay buffer is related to the effects of microstructure of bentonite on the flow of water and transport of chemicals (Yong, 2003). Comparisons between the results of modelling investigations and experimental data have highlighted the importance of microstructure processes in moisture flow in compacted bentonite (e.g. Thomas et

al., 2003; Sánchez et al., 2012; Thomas and Sedighi, 2012). Theoretical approaches have been proposed to describe the effects of microstructure deformation (expansion/shrinkage) on hydraulic or hydro-mechanical behaviour of compacted bentonite (e.g. Thomas et al., 2003; Kröhn, 2003; Xie et al., 2004; Sánchez et al., 2012; Navarro et al., 2014). The effects of clay-water-chemical interactions are also manifested in the transport of chemicals as experimental studies show that the effective diffusion coefficients of ionic species vary considerably with the type of chemical species in the compacted bentonite (e.g. Kozaki et al., 2001; Muurinen et al., 2007; Van Loon et al., 2007; Wersin et al., 2004). In this study we consider the effects of microstructure of compacted bentonite and its evolution on moisture flow and chemical transport. We adopt a new approach proposed by Sedighi and Thomas (2014) by which the hydration and dehydration of microstructure of compacted bentonite and its associated porosity are calculated directly from thermodynamics of hydration/dehydration of smectite.

A summary of the governing formulations and the numerical model is first presented. The procedure of analysis, material properties, initial conditions and boundary conditions applied in the simulations are discussed in detail. The results of simulations are presented that include two stages of analysis: i) the *transient analysis* of evolution of thermal, hydraulic and chemical/geochemical variables in the domain under the same conditions that have been applied in the heating and hydration tests by Villar et al. (2008b) and ii) the *post-mortem* geochemical analysis of the results from stage i) that are based on the same thermal and hydraulic conditions applied in the geochemical *post-mortem* analysis as reported by Fernández and Villar (2010). The results are compared with those reported from the experimental tests, enabling to identify key hydro-geochemical processes involved during the test and examine the accuracy of the model under the conditions of the application case.

2. Coupled thermal, hydraulic and chemical formulations and numerical model

The numerical investigation presented was carried out by extending the capabilities and theoretical aspects of a coupled thermal, hydraulic, chemical and mechanical model (THCM) (COMPASS) (e.g. Thomas and He, 1997; Seetharam et al. 2007; Vardon et al., 2011; Sedighi et al., 2016) through i) development of a theoretical formulation for multicomponent chemical transport under coupled

thermo-hydraulic conditions (Sedighi et al, 2011; Thomas et al., 2012), ii) inclusion of microstructure effects in transport phenomena by developing a chemistry-based micro porosity evolution model (Sedighi and Thomas, 2014) and iii) integration of the geochemical model PHREEQC into the transport model to form an integrated reactive transport model under coupled THCM formulation (i.e. COMPASS-PHREEQC) (Sedighi et al., 2015; Sedighi et al. 2016).

The processes considered in the governing equations of the model are: i) heat transfer via conduction, convection and latent heat of vaporisation, ii) moisture (water and vapour) flow due to thermal and hydraulic driving potentials, iii) transport of multicomponent chemicals via advection, dispersion and diffusion mechanisms and iv) heterogeneous and homogenous geochemical reactions that can occur in the soil, water and air system.

2.1. Heat transfer and moisture flow

The governing equation for heat transfer considers the energy conservation given as (Thomas and He, 1997):

$$\frac{\partial [H_c(T - T_r)\delta V + L\rho_v\theta_a]}{\partial t} = -\delta V \nabla \cdot [-\lambda_T \nabla T + L(\rho_l \mathbf{v}_v + \rho_v \mathbf{v}_a) + A(T - T_r)] \quad (1)$$

where, H_c is the heat storage capacity. T and T_r represent temperature and the reference temperature, respectively. t is time and δV represents the incremental volume, L represents the latent heat of vaporisation. θ_a is the volumetric air (gas) content. ρ_l and ρ_v are the water and vapour density, respectively. \mathbf{v}_v and \mathbf{v}_a represents the vapour velocity and air velocity, respectively. λ_T is the thermal conductivity and A stands for the sum of the heat convection components. Further details related to heat transfer parameters can be found in Thomas and He (1997).

The governing equation for moisture flow is based on mass conservation law. The flow of water (liquid) in unsaturated porous medium is explained using Darcy's law and the vapour flow is considered to be driven by diffusion and advection processes (Thomas and He, 1997):

$$\frac{\partial (\rho_l \theta_l \delta V)}{\partial t} + \frac{\partial (\rho_v \theta_a \delta V)}{\partial t} = -\delta V \nabla \cdot (\rho_l \mathbf{v}_l + \rho_l \mathbf{v}_v + \rho_v \mathbf{v}_a) \quad (2)$$

where, θ_l is the total volumetric liquid content. \mathbf{v}_l represents the water velocity.

By considering capillary and gravitational potentials, the liquid flux, in an expanded form can be written as (Thomas and He, 1997):

$$\mathbf{v}_l = k_l \left(\frac{\nabla u_l}{\rho_l g} + \nabla z \right) \quad (3)$$

where, k_l is the unsaturated hydraulic conductivity of soil. u_l is the pore water pressure. g is the gravitational constant and z stands for the elevation.

The diffusive component of the vapour flow is considered based on the formulation proposed by Philip and de Vries (1957):

$$\mathbf{v}_v = \left[\frac{D_{atms} v_v \tau_v (1 - \theta_l)}{\rho_l} \rho_0 \frac{\partial h}{\partial s} \right] \nabla u_l - \left[\frac{D_{atms} v_v}{\rho_l} f \frac{(\nabla T)_a}{\nabla T} \left(h \frac{\partial \rho_0}{\partial T} + \rho_0 \frac{\partial h}{\partial T} \right) \right] \nabla T \quad (4)$$

where D_{atms} is the molecular diffusivity of vapour through air, τ_v is the tortuosity factor, v_v is a mass flow factor. ρ_0 is the density of saturated water vapour, h is relative humidity and s represents total suction. $\left[\frac{(\nabla T)_a}{\nabla T} \right]$ denotes the microscopic pore temperature gradient factor and f is a flow area factor . The flow factor reduces the vapour flow since the available flow area decreased at high moisture contents.

Further details related to moisture transfer equations can be found in Sedighi (2011) and Sedighi et al. (2016).

2.2. Reactive transport of multicomponent chemicals

The formulations of reactive transport of chemicals are based on mass conservation. The geochemical reactions causing gain or loss of each chemical component are considered via a sink/source term in the transport formulation. The transport formulation considers the transfer mechanisms of advection, diffusion and dispersion of multiple chemicals in the liquid phase.

It has been shown that anionic and cationic species diffuse at different rates in multi-ionic aqueous system of compacted smectite. Therefore, the diffusion rate of each ion may deviate from that calculated by the Fick's diffusion law (Lasaga, 1979). It is therefore required that the condition of electro-neutrality of the aqueous system should be implemented in the transport formulation of

multiple ions. Sedighi et al. (2011) and Thomas et al. (2012) have presented a general formulation for chemical transport in multi-ionic systems. The formulation considers diffusion under combined molecular diffusion and thermal diffusion and satisfies the electro-neutrality condition of the pore fluid system (a summary of the formulation is presented in Appendix A). It is noted that the formulation only considers flow in the bulk fluid, i.e. the transport of chemicals does not include diffusion via surface diffusion or interlayer diffusion processes.

The mass conservation alongside electro-neutrality condition has been adopted to develop the governing equation for the transport:

$$\frac{\partial(\theta_l c_i \delta V)}{\partial t} + \frac{\partial(\theta_l s_i \delta V)}{\partial t} = -\delta V \nabla \cdot \left(c_i \mathbf{v}_l - \sum_{j=1}^{n_c} \theta_l \tau_i D_{ij} \nabla c_j - \theta_l \tau_i D_i^T \nabla T - \mathbf{D}_m \nabla c_j \right) \quad (5)$$

where, c_i is the concentration of the i^{th} chemical component, s_i a geochemical sink/source term which stands for the amount of the i^{th} chemical component that is produced or depleted due to geochemical reactions. D_{ij} is the effective molecular diffusion coefficient of the i^{th} chemical due to the chemical gradient of the j^{th} chemical component, D_i^T represents the thermal diffusion coefficient of the i^{th} chemical. \mathbf{D}_m is the matrix of the effective dispersion coefficients. τ_i is the tortuosity factor of the i^{th} chemical component.

The molecular diffusion and thermal diffusion coefficients can be presented as (Thomas et al., 2012):

$$D_{ij} = -\delta_{ij} D_i^0 \left(1 + \frac{\partial \ln \gamma_i}{\partial \ln c_i} \right) + \frac{z_i D_i^0 c_i}{\sum_{k=1}^{n_c} z_k^2 D_k^0 c_k} z_j D_j^0 \left(1 + \frac{\partial \ln \gamma_j}{\partial \ln c_j} \right) \quad (6)$$

$$D_i^T = -D_i^0 c_i \frac{Q_i^{*0}}{RT^2} + \frac{z_i D_i^0 c_i}{\sum_{k=1}^{n_c} z_k^2 D_k^0 c_k} \sum_{j=1}^{n_c} z_j c_j D_j^0 \frac{Q_j^{*0}}{RT^2} \quad (7)$$

where, δ_{ij} is the Kronecker's delta. D_i^0 is the self-diffusion coefficient of the i^{th} chemical component in free water. z_i stands for the ionic valence of the i^{th} chemical component and Q_j^{*0} is the heat of transport of the j^{th} chemical component.

The components of geochemical sink/source term presented in the governing equation of chemicals are calculated using a geochemical model which was linked to the model. This was achieved by coupling the geochemical model PHREEQC version 2 (Parkhurst and Appelo 1999) with the transport model (Sedighi et al., 2016). In relation to the application considered in this work, the geochemical modelling features that were coupled to the transport model and tested include i) equilibrium reactions, applied to precipitation/dissolution of minerals, ii) kinetically controlled reactions, applied to precipitation/dissolution of minerals and iii) Ion exchange processes, considered under equilibrium conditions.

2.3. Numerical model

The numerical solution to the formulations of the heat transfer, moisture flow and chemical transport has been achieved by the application of the finite element method and the finite difference method (Thomas and He, 1997; Seetharam et al., 2007). The Galerkin weighted residual method has been adopted by which the spatial discretisation is developed.

The solution adopted for the reactive transport formulation of chemicals is based on an operator splitting approach in which the governing equations for the transport (and mechanical) formulation and the geochemical reactions are solved sequentially (Steefel and MacQuarrie, 1996). The operator splitting approach has been extensively adopted in the development of reactive transport models in various forms including sequential iterative approach (SIA), sequentially non-iterative approach (SNIA) and sequentially partly-iterative approach (SPIA). Examples of established reactive transport codes are *HYDROGEOCHEM* (Yeh and Tripathy, 1991), *CrunchFlow* (Steefel and Molins, 2016); *PHREEQC* (Parkhurst and Appelo, 1999), *THOUGHREACT* (Xu et al., 2004), HPx (Jacques and Šimůnek, 2005), CORE 2D (Samper et al., 2009) that adopt operating splitting approaches and are widely applied in various fields.

In order to couple the chemical transport model and the geochemical reaction model (calculated by PHREEQC version 2), a sequential non-iterative approach (SNIA) was adopted. In summary, the chemical transport equations are separately solved at each time step and the concentrations of

chemicals calculated are then used for the geochemical modelling using PHREEQC. The values of dissolved chemical concentrations corrected after the geochemical modelling are returned into the transport module for the next step of analysis. The coupled reactive transport model presented here has carefully been tested and verified against several benchmarks that are presented in details elsewhere (Sedighi et al., 2016). Appendix B provides a description of the numerical and computational aspects of the model.

3. Case study and simulation details

The case study presented here is based on a series of heating and hydration experiments on FEBEX bentonite, compacted at dry density around 1650 kg/m^3 reported by Villar et al. (2008a,b) that have been carried out for a period of 0.5 to 7.6 years. As shown in Figure 2, the experimental tests included the hydration of compacted clays samples by an aqueous solution from the top of the sample at 1.2 MPa (infiltration pressure) and at ambient temperature (20-30 °C) while an elevated temperature has been applied at the bottom of the cell (100 °C). The size of the cylindrical samples was 600 mm (height) and 70 mm (diameter).

An axi-symmetric analysis has been carried out on a discretised domain to 500 unequally sized elements (4-noded axi-symmetric elements). In order to prevent numerical instability and improve the convergence, the first 200 mm in the heating side (bottom) and the hydration side (top) of the sample were discretised into smaller elements (equally sized 1 mm elements). Equally sized 2 mm elements were used in the 200 mm distance in the middle of domain. The maximum time-step allowed in the numerical analysis was 500,000 seconds. The time steps were allowed to the maximum allowed value by a rate of 1.05. If the convergence criteria are satisfied within a specified numbers of iterations, the time-step was allowed to increase otherwise, the time-step was reduced to a lower value to achieve convergence.

Geochemical analysis of the pore fluid composition at the initial water content (14% gravimetric) and temperature at 25 °C was carried out using PHREEQC by considering the equilibration of the whole clay-water system with pure water at pH 7.72 and atmospheric CO_2 partial pressure ($\text{PCO}_2 \approx 10^{-3.5}$).

The quantities of the soluble minerals and exchangeable cation contents of the bentonite were adopted from the average values for the FEBEX bentonite provided by Fernández et al. (2001). Following Fernández et al. (2001), dissolution-precipitation of minerals including calcite, halite and gypsum and ion exchange reactions was considered in the modelling. The coefficients for exchange reactions reported in ENRESA (2000) were employed. For mineral reactions the database of PHREEQC (phreeqc.dat) was used. A summary of the thermodynamics parameters of mineral dissolution/precipitation and ion exchange reactions is provided in Table 1. The results of geochemical modelling of the pore water composition are presented in Table 2. The chemical composition of the aqueous solution injected to the system is also presented in Table 2.

A coupled thermal, hydraulic and chemical analysis was carried out to obtain the *transient* evolution of key variables in the domain that include temperature, pore water pressure, ionic species in the pore fluid and a set of geochemical variables in the domain including minerals, exchangeable ions and pH. (Referred as the *transient analysis*). Figure 3 shows the thermal, hydraulic and chemical initial and boundary conditions applied that were adopted based on the conditions of the experiments. Constant temperature and water pressure at the top of the domain equal to 298 K and 1.2 MPa, respectively, was considered. A fixed temperature equal to 373 K and impermeable boundary condition to water flow was applied at the bottom of the domain. The boundary conditions for the chemical components at the top of the domain were considered to be fixed concentration whilst at the bottom of the domain, an impermeable boundary was considered. At the radial boundary, a heat flux was applied, representing the potential heat loss from the cell. The heat loss can theoretically be calculated that is equal to 2.3 W/m²/K. This value is obtained by considering a 15 mm PTFE casing having thermal conductivity of 0.25 and 15 mm foam insulation with thermal conductivity of 0.4 W/m/K (Villar et al. 2008b). A lower value of heat flux, i.e. 1.78 W/m²/K, was used in the simulation compared with the calculated theoretically due to potential layer of air trapped in the radial boundary of the sample that may have provided an extra isolation layer. The radial boundary is considered to be impermeable to fluid. Precipitation/dissolution of calcite has been considered as a kinetically controlled reaction in the *transient analysis* whilst mineral reactions have been considered as equilibrium reaction for other

minerals involved. The kinetic rate of calcite reaction was adopted from the equation and parameters presented in the phreeqc.dat data base of PHREEQC.

The water content and temperature applied during the experimental post-mortem geochemical analysis were 400% gravimetric water content (i.e. the ratio of liquid/solid was 4:1) and 25 °C, respectively (Fernández and Villar, 2010). These values can be different from the water content and temperature at the corresponding locations in the sample after the completion of experimental tests or transient analysis (0.5, 1.0, 2.0 and 7.6 years). Changes in the water content and temperature during post mortem tests will affect the geochemical equilibrium of the soil-chemical-water system; hence the composition of ions resulting from the transient analysis at the end of the tests should be re-analysed to replicate the experimental conditions (water content and temperature) in which the post mortem experiments were carried out. This step of analysis (post mortem analysis) will enable the comparison of transient analysis with post mortem experiments, i.e. provide a validation. The results of numerical simulations including temperature, water content and geochemical variables obtained from *transient analysis* at 0.5, 1.0, 2.0 and 7.6 years were used as initial inputs for calculating the pore water composition of the samples using PHREEQC under the water content and temperature of post mortem experimental conditions of the experiments (i.e. 25°C and 400% gravimetric water content).

In summary, the experimental data used to develop the simulations and comparison with the results of analysis include i) *transient* temperature profile and ii) water contents profile and pore fluid chemistry based on the geochemical *post-mortem* analysis at the end of the tests reported.

4. Material properties

4.1. Thermal and hydraulic behaviour

The material constants including density of water, density of solid, specific heat capacity of solid, liquid and vapour, latent heat of vaporisation, Henry's constant and specific gas constant for gas vapour were obtained from the literature (Mayhew and Rogers, 1976 and ENRESA, 2000). The value reported by ENRESA (2000) was used for the reference thermal conductivity of compacted FEBEX bentonite. The moisture retention relationship used is based on the van Genuchten's equation (van

Genuchten, 1980) and the parameters provided in ENRESA (2000) for compacted FEBEX bentonite. Table 3 presents a summary of key thermal and hydraulic properties adopted for the simulations. Using the moisture retention relationship provided, the initial degree of saturation (58.6%) corresponds to a suction value equal to approximately 90.0 MPa.

As discussed in the introduction section, studies of the hydraulic behaviour of compacted bentonite have indicated that the expansion/shrinkage of the clay microstructure during hydration/dehydration show profound effects and control on the moisture flow in compacted bentonite (e.g. Thomas et al., 2003; Sánchez et al., 2012). As shown in Figure 3, the porosity system of compacted bentonite can be conceptualised at least by two scales of porosity (Sedighi and Thomas, 2014): i) “micro porosity” that comprises the pore spaces between the unit layers of smectite or lamellas, (also called interlayer porosity) and ii) “macro porosity” that includes pores between the particles (inter-particle pores) and between the aggregates of particles (inter-aggregate pores). “Micro porosity” is always fully saturated and hydration and dehydration processes, therefore, changes the interlayer distance between the clay platelets by adding/removing water molecules. The interlayer hydration and dehydration of smectite involves adsorption or desorption of one to three discrete layers of water molecules between the clay platelets (Push and Yong, 2006). The crystalline structure of the mineral remains unchanged during the hydration/dehydration process (Ransom and Helgeson, 1994). The water molecules within the interlayer space of smectite (micropores), combined with a small portion of water attached to the particle external surfaces, constitutes a proportion of water that is considered to be immobile compared with that located in macropores (Pusch et al., 1990; Hueckel, 1992). The pathways for water flow and transport of ionic-species in compacted bentonite are practically reduced to the spaces/pores between the particle and aggregates. The macro porosity is (in contrast to the micro porosity) a two-phase system that can contain both liquid and vapour. Water molecules can be exchanged between these two scales of porosity.

Thomas et al. (2003), Sedighi (2011) and Thomas and Sedighi (2012) have introduced a form of modified hydraulic conductivity that includes the effects of microstructure swelling on hydraulic conductivity. The concept is based on the assumption that the porosity available to water flow is

limited to the macro pore spaces between the clay particles and the water that exists in the interlayer porosity is practically immobile. A general form of the modified relationship for the hydraulic conductivity of compacted bentonite is given as follows (Sedighi, 2011):

$$k_l = \left(1 - \frac{\theta_{il}}{\theta_l}\right) k_{sat} S_l^\beta \quad (8)$$

where, k_{sat} is the saturated hydraulic conductivity ($k_{sat} = 3.5 \times 10^{-14}$ m/s for compacted FEBEX bentonite) and β is a constant which has been given as 3 for the studied clay (Villar et al., 2008a). θ_{il} is the volumetric water content of microstructure (interlayer volumetric water content).

The formulation of moisture flow (mass balance) has been applied to the total water content (sum of the moisture content in micro pore and macro pore). We do not consider a separate mass balance equation for the micro pore water evolution as i) we consider water in the interlayer to be immobile and ii) we consider the system under equilibrium (i.e. mass exchange between the micro and macro is instantaneous). The effect of micro porosity evolution is manifested in the water flux by the hydraulic conductivity relationship that includes implicitly the effects of microstructure. It is noted that a double porosity approach with an exchange term that considers a kinetically controlled exchange of water between micro and macro pores would provide a more comprehensive approach. However, this was beyond the scope of current study.

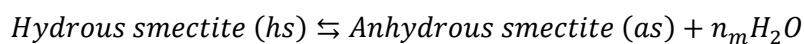
Comparisons between the experimental results and simulations that consider the modified hydraulic conductivity in hydraulic flow formulations show a closer correlation with the behaviour observed in experimental studies of both isothermal and non-isothermal water infiltration (Sedighi, 2011; Thomas and Sedighi, 2012). Section 4.2 describes the approach developed to calculate the interlayer water content.

4.2. Microstructure evolution during hydration and dehydration

Compaction of bentonite primarily reduces the macro porosity (Likos and Lu, 2006). Therefore by increasing the dry density of compacted bentonite, it is expected that the contribution of interlayer

porosity to the overall porosity increases. During hydration of smectite, a number of discrete layers of water are entered into the variable pore space between the individual unit layers of smectite (interlayer porosity). A maximum number of 3 to 4 layers of water molecules can be adsorbed in the smectite interlayer that correspond to the basal spacing of approximately 1.70 to 2.0 nm, respectively (Laird, 2006). Models for prediction of the interlayer/micro porosity variation in compacted bentonite are very limited (especially under variable suction or temperature). The existing prediction are based on the variation of basal spacing between the interlayer platelets, observed in the XRD analysis by which the porosity associated can be calculated by considering a homogeneous distribution of parallel clay platelet in the system (Likos and Lu, 2006; Warr and Burger, 2007; Likos and Wayllace, 2010; Holmboe et al., 2012).

Sedighi and Thomas (2014) have proposed a generic approach to calculate the interlayer porosity/interlayer water content of compacted bentonite and its evolution with environmental conditions (relative humidity and temperature) based on a geochemical model of hydration/dehydration of smectite proposed by Ransom and Helgeson (1994). The interlayer hydration and dehydration of smectite can be described as a geochemical reaction between water molecules and a symbolic hydrous and its homologous anhydrous counterparts of smectite (Ransom and Helgeson, 1994; Vidal and Dubaqt, 2009): described as:



where, n_m is the number of moles of water present in the interlayer adsorption or desorption reaction, given as the moles of water per smectite half formula unit, i.e. $O_{10}(OH)_2$ (Ransom and Helgeson, 1994).

Ransom and Helgeson (1994) have shown that solid solution reaction of interlayer hydration/dehydration can be expanded as (Ransom and Helgeson, 1994):

$$\log K_{eq} = \log \left(\frac{1 - X_{hs}}{X_{hs}} \right) + \frac{W_s}{2.303RT} (2X_{hs} - 1) + n_m \log a_w \quad (9)$$

where, K_{eq} represents the equilibrium constant of the reaction and X_{hs} represents the mole fraction of the hydrous smectite. W_s denotes the Margules parameter for the binary regular solid-solution of hydrous and anhydrous smectite components at reference temperature (25 °C) and pressure (0.1 MPa) which is independent of pressure and temperature (Ransom and Helgeson, 1994). R refers to gas constant. a_w is the activity of water.

Sedighi and Thomas (2014) have shown that the interlayer porosity/interlayer water content that is calculated as a function of the mole fraction of hydrous smectite in the interlayer hydration/dehydration reaction of smectite. Accordingly, the interlayer volumetric water content can be given as (Sedighi and Thomas, 2014):

$$\theta_{il} = X_{hs} \frac{n_m v_{il}}{m_{sm}} \rho_d^{sm} \quad (10)$$

where v_{il} denotes the specific molar volume of the interlayer water, m_{sm} is the molar mass of dry smectite and ρ_d^{sm} represents the bulk dry density of smectite.

It is noted that as the interlayer space remains always saturated. Therefore, the porosity associated with the microstructure (n_{il}) is equivalent to the interlayer volumetric water content (θ_{il})

Based on equation (9), the mole fraction of hydrous smectite can be calculated by knowing the equilibrium constant of the reaction ($\log K_{eq}$), the Margules parameter (W_s) and the mole number of hydrate water in a fully hydrated smectite (n_m) at given temperature (T) and water activity (a_{H_2O}).

Assuming the molar volume of interlayer water to be same the same as that in macro pore, the activity of water can be expressed in terms of the relative humidity (or total suction) of the macro pore or the surrounding environment.

The thermodynamic parameters of the solid-solution model for pure smectites, including the equilibrium constants of the reactions and the Margules parameters were reported by Ransom and Helgeson (1994). The parameters have been derived based on calibration of the model against laboratory based vapour adsorption data of powdered smectite samples. The equilibrium constant of

the reaction ($\log K_{eq}$) varies with temperature (Ransom and Helgeson, 1995) that is calculated as a function of the standard enthalpy of reaction ($\Delta H_{r,T_r}^0$) at reference temperature (T_r) and the standard heat capacity of the reaction at constant pressure, (ΔC_p^0) given as (Langmuir, 1997):

$$\log K_{eq} = (\log K_{eq})_{T_r} + \frac{\Delta H_{r,T_r}^0}{2.303R} \left(\frac{1}{T_r} - \frac{1}{T} \right) + \frac{\Delta C_p^0}{2.303R} \left(\frac{T}{T_r} - 1 \right) + \frac{\Delta C_p^0}{2.303R} \ln \left(\frac{T}{T_r} \right) \quad (11)$$

In this study we adopted the thermodynamic parameters for the hydration/dehydration reactions for homo ionic smectite presented by Ransom and Helgeson (1994) considering FEBEX bentonite as a mixture of Ca, Mg and Na smectite. Table 4 present a summary of the parameters used to calculate the micro porosity variation.

4.3. Chemical transport behaviour

Two series of parameters required for modelling the reactive transport of chemicals include i) transport properties and ii) thermodynamic and kinetic parameters of the geochemical reactions. The latter has been described in section 2 and the parameters used have been detailed in Table 1. The transport parameters required are those related to the molecular diffusion and thermal diffusion processes in according to Equations 5 to 7.

García-Gutiérrez et al. (2004) studied the diffusion properties of FEBEX bentonite and have shown that the accessible porosity for HTO agrees well with the total porosity, which implies that all the pores in compacted bentonite are available for diffusion of neutral species. The accessible porosity for the diffusion of chloride tracer was reported to be considerably smaller than the total porosity, even at the lower densities, demonstrating a significant anionic exclusion. Their results indicated that the accessible porosity for chloride is a small fraction of total porosity (2-3 %) at a dry density of 1650 kg/m³. The tortuosity factors for anionic and cationic species (τ_i) were therefore considered to be different in this study. The effects of tortuous path and constrictivity (together) were included by considering different effective porosities for diffusion of anionic and cationic species. A modified form of the tortuosity factor proposed by Revil and Jougnot (2008) was used in which the porosity is replaced by the effective porosity. The relationship used to describe the tortuosity factor is:

$$\tau_i = (n_{eff}^i)^{\beta-1} (S_l - S_l^c)^{\gamma-1} \quad (12)$$

where n_{eff}^i is the effective porosity for diffusion of the i^{th} ionic species. S_l^c is the percolation threshold for degree of saturation, suggested by Revil and Jougnot (2008). β and γ are constants. In this study the values of S_l^c , β and γ were considered to be 0, 2.5 and 2.75, respectively.

The effective porosity for the anionic diffusion is described by:

$$n_{eff}^{Anions} = n - n_{il} - n_{DDL} \quad (13)$$

where n_{il} represents the interlayer porosity calculated from the hydration/dehydration model (based on Equation (10) and n_{DDL} is the porosity associated with the developed diffusion layer.

The effective porosity for chloride diffusion has been given in the range of 0.02-0.03 for fully saturated FEBEX bentonite, compacted at dry density of 1650 kg/m³ (García-Gutiérrez et al., 2004). Applying Equation (9) under saturated state and ambient temperature yields the interlayer porosity to be approximately 0.27. The porosity associated with the developed diffusion layer was calibrated as a constant value of 0.105 for the anionic species to produce the effective porosity in the range of 0.02-0.03 at saturated state based on effective porosity values provided by García-Gutiérrez et al.(2004) (i.e. $n_{eff}^{Anions} = 0.4 - 0.27 - 0.105 = 0.025$). Including the above tortuosity factor and volumetric water content using Equation (9), the corresponding value for the effective diffusion coefficient for chloride in fully saturated FEBEX bentonite compacted at dry density of 1650 kg/m³ is obtained equal to 1.27×10^{-12} m²/s which is close to the experimentally measured value of 1.1×10^{-12} m²/s (García-Gutiérrez et al. 2004). For all anionic species the same tortuosity factor was applied. The effective porosity of cations was assumed to be the effective porosity for water tracer (HTO) diffusion, given as the total porosity in compacted bentonite soils (García-Gutiérrez et al., 2004). The rate of diffusion rate of cations in compacted bentonite has been reported to be larger than that of HTO and this has been explained to be related to the interlayer diffusion or surface diffusion. It is noted that, in the modelling study presented here, enhanced diffusion rate of cations through potential mechanism such as interlayer or surface diffusion has not been considered. By applying the total porosity to the

tortuosity factor presented in Equation (15), the effective diffusion coefficient for cations is obtained in the range of 6.32×10^{-11} to 1.56×10^{-10} m²/s. These values are also in agreement with the values reported for HTO effective diffusion coefficient equal to 5.8×10^{-11} m²/s, for fully saturated compacted FEBEX bentonite at dry density of 1650 kg/m³ (García-Gutiérrez et al., 2004).

Thermal diffusion of multicomponent chemicals is considered in accordance to the formulation provided in Equation (5). The term heat capacity in Equation (7) is calculated using the theoretical approach proposed by Agar et al. (1989) as:

$$Q_i^* = Az_i^2 D_i^0 \quad (14)$$

where, A is a constant value that depends on the hydrodynamic boundary condition (i.e. 2.48×10^{12} and 2.20×10^{12} for two different hydrodynamic boundary conditions). An average value of the two hydrodynamic boundary conditions was used for this parameter. Details can be found in Sedighi et al. (2011) and Thomas et al. (2012).

The self-diffusion coefficients of the ionic species in water at 25 °C (D_i^0) were taken from the values reported by Lasaga (1998). The Stokes-Einstein relationship has been used to obtain the self-diffusion coefficient of ions in water at variable temperature (Cussler, 1997).

Chloride ion is the dependent component considered in the transport model in relation to the overall charge conservation requirement as explained in Appendix A. In other words, the chemical transport formulation is solved for all chemical components except Cl⁻. The concentration of chloride is then calculated from the “no net charge” condition $\sum_{i=1}^{n_c} \frac{\partial(\theta_l z_i c_i \delta V)}{\partial t} = 0$ (Appendix A). The charge-balance condition in the geochemical reaction ($\sum_{i=1}^{n_c} \frac{\partial(\theta_l z_i s_i \delta V)}{\partial t} = 0$) is also separately satisfied during reaction modelling by PHREEQC by adjusting the pH (i.e. The charge-balance equation is used to calculate pH in batch reactions by PHREEQC).

5. Results and discussion

The results of numerical simulations of heat transfer, moisture flow and reactive transport of chemicals are presented in this section. In terms of temperature evolution in the domain, the results of

the *transient analysis* are compared with the transient results of temperature monitoring from the experiment. The variations of water content are compared with those reported from the post mortem analysis by Villar et al. (2008b). In terms of chemical behaviour, the results of two series of analysis are presented: 1) the results of *transient analysis* from coupled numerical simulations that demonstrate the possible state of soil-water-chemical system at the end of 0.5, 1, 2 and 7.6 years experimental tests and 2) the results of *post mortem analysis* that are used to compare against data from the post mortem geochemical experiments provided by Fernández and Villar (2010).

5.1. Thermal and hydraulic behaviour

Figure 4 presents the results of temperature evolution in the domain and those reported by Villar et al. (2008b). Thermal processes reach relatively quickly the steady state and temperature distribution in the domain remains under stable condition for the periods of analysis. The numerical results agree well with the experimental results. Variations of the degree of saturation are presented in Figure 5. The experimental profiles of moisture content and dry density in the domain reported by Villar et al. (2008b) were used to compare the variations of the degree of saturation in the domain. It is noted that the porosity was considered to be constant (0.4) to calculate the degree of saturation from water content data reported. From Figure 5, it can be observed that there is a close agreement between the numerical and experimental results. However, the numerical model has slightly under-predicted the drying at the hot boundary region for the periods of 6, 12, 24 months but well correlated in the case of 92 months. In the hydration side, the model predicted slightly higher degree of saturation up to 24 months. However, the results are correlated well with the experimental results for the period of 92 months analysis. The parameters used in the vapour transport model, which generally yield higher vapour flux due to temperature gradient, can be described as reasons behind the higher drying obtained close to the hot boundary. Theoretical understanding of unsaturated bentonite behaviour under elevated temperatures is immature due to the degree of complexity and coupling between different processes. The comparison presented highlights the need for further research at lower scales of modelling (i.e. pore scale) that can reduce the level of uncertainty in parameters that are conventionally used in modelling at continuum scale.

The rate of hydration due to the injecting fluid has been gradually reduced and the results correlate with the results of experimental hydration front for the duration of 92 months. This is mainly due to the application of the modified hydraulic conductivity through the interlayer modification factor (i.e. $(1 - \frac{\theta_{il}}{\theta_l})$ in Equation 8). The interlayer hydration process reduces the hydraulic conductivity as the interlayer water ratio approaches higher values. Although the soil deformation was not considered and simulated, the effects of changes in the available porosity for the water flow and transport of chemicals have been considered through the modification of the hydraulic conductivity.

Based on the experimental results (Villar et al., 2008b), the dry density of the samples has changed from an initial value of 1650 kg/m³ to a maximum range of 1700 to 1750 kg/m³ in the vicinity of heater. In the hydration side, the dry density has reduced to a minimum value of 1400-1450 kg/m³. The total porosity has theoretically be reduced to 0.35 close to the heater and increased to 0.47 in the hydration boundary from its initial value of 0.4. It is therefore anticipated that the overall effects of porosity variation on the flow behaviour in the heater zone are limited. Since the overall swelling of sample was constrained, the increase of porosity in the hydration affected area has reduced the macro porosity that has been captured in the model via modified hydraulic conductivity relationship used. The deformation effects are likely to be less effective on the overall transport behaviour, acknowledging the fact that moving towards understanding the swelling pressure development in the system and accurate description of the coupled processes, mechanical behaviour is important.

5.2. Chemical behaviour - Anionic species

Figure 6 presents the profiles of chloride (Cl⁻) distribution in the domain at different times. Chloride can be considered as a conservative anion, it is not commonly involved in geochemical reactions and not affected by changes in the pH and redox conditions. Therefore the chloride distribution in the domain has not been affected by the geochemical reactions during the *post-mortem analysis*. The chloride profile related to the *transient analysis* and *post-mortem analysis* yielded exactly same values as it was expected (Sedighi, 2011). The results of post mortem experiments reported by Fernández and Villar (2010) are also shown in Figure 6. Accumulation of chloride towards heater that is

associated with the advective flow of chloride ions, flushed towards the heater from the hydration boundary. The accumulation of the chloride ions in the first 200 mm distance from the hydration side is also observed. The front peak in chloride profile is extended towards the middle of the domain with time. Moreover, due to the increase in temperature in the areas close to the heater, the liquid water moves towards the heater. Chloride ions in the domain have been transferred towards the heater by the liquid water flow from the boundary that is an advective dominated process. Moisture transfer can simultaneously take place from the hot end towards the cold region in the form of vapour. Water evaporates whilst approaching the heater due to higher temperature and diffuses towards the colder side until it condensates at further distance from the heater. Consequentially, as the pores close to the heater are less saturated suctions are established. Water then moves toward the heater via advective liquid flow due to the suction gradient. At any location, thermodynamics equilibrium between the water in the form of liquid and vapour should be achieved at certain temperature of the studied point in the domain. The chloride ions carried by the liquid flow remained at the hot end, as the moisture content reduces due to the vapour flow induced by elevated temperature. The process of simultaneous water and vapour movement in the areas close to the heater is anticipated to be responsible for the excess accumulation of chloride close to the heater while the chloride content was reduced from the initial amount in the area of approximately 80 to 300 mm away from the heater.

The magnitudes of the accumulation peaks of chloride in the area of hydration side are also close to the experimental results for the periods of 6, 12 and 24 months. The results for the first three periods of analysis indicate a similar pattern for the chloride distribution in the vicinity of heater and in the distance of 100-200 mm away from the heater, respectively. However, the results of model for the 92 months analysis show a higher amount of chloride in the area of 100-300 mm in the vicinity of the hydration side compared with the experimental results. The model predicted smaller quantities of chloride close to the heater. The experimental results show that chloride was almost removed from the more hydrated 400 mm of bentonite, whereas its concentration showed a sharp gradient in the 200 cm closest to the heater. This observation suggests that there can be further processes involved in controlling the hydraulic conductivity evolution that is not fully captured by the hydraulic

conductivity model adopted. This includes the thermally coupled processes such as thermal osmosis (e.g. Zagorščak et al. 2016).

Figure 7 presents the distribution profiles of sulfate (SO_4^{2-}) in the domain obtained from the transient numerical analysis and post mortem analysis. The distribution of the dissolved sulfate in the case study is controlled by i) the flow processes associated with thermal and hydraulic variations and ii) mineral reactions involving gypsum and anhydrite. The domain initially contained some gypsum but no anhydrite. The concentration of sulfate has reduced by advancing the hydration front and gypsum has been dissolved that is controlled by the amount of sulphate ions. The results of gypsum distribution in the domain, presented in Figure 8, indicate that almost all gypsum was dissolved in 50 mm distance from the hydration boundary. The peak of leached sulfate in the hydration side is also located in the same region where gypsum has been dissolved. High and constant concentration of sulfate is observed for the distance of approximately 250 mm distance between 50 mm to 300 mm away from the hydration end that is due to the gypsum dissolution according to the results presented in Figure 5. The amount of sulfate shows a decrease in the areas close to the heater. This is believed to be related to the precipitation of anhydrite as it can be seen in Figure 8. The equilibrium constant of mineral reactions for gypsum and anhydrite are very close whilst their enthalpies of reaction are different, leading to a different behaviour of these two minerals at the regions with higher temperature. The distribution of the dissolved sulfate close to the heater is believed to be attributed to the precipitation of anhydrite due to the higher temperature in the domain. Based on the results presented in Figure 8, a considerable amount of anhydrite has been precipitated in the vicinity of heater.

Figure 7 presents a comparison between the results of post-mortem analysis and experiments for the dissolved sulfate in the domain. There is a qualitative agreement in terms of distribution pattern between the model and experimental results. In the area of hydration, numerical model predicted the sulfate contents close to the experimental results. However the locations of peaks are slightly different in the model compared with the experimental results. The model shows an over-prediction at the hot end and an under-prediction in the area close to the hot end, affected by the coupled thermally

induced liquid-vapour movement. It is anticipated that the over-prediction at the hot end is due to the high amount of anhydrite precipitation in the transient numerical modelling results.

Figure 9 shows the results of transient simulation and post mortem analysis for the dissolved bicarbonate (HCO_3^-). Bicarbonate ions have been transferred to the domain by the water at the hydration boundary that has resulted in accumulation of bicarbonate in a limited region close to the boundary. As shown in Figure 10, the overall amount of calcite has not significantly changed for different periods of analysis compared to the initial value. This is due to the low rate of precipitation/dissolution of calcite. Localised precipitation of calcite has occurred in the vicinity of heater as results of lower initial concentrations of bicarbonate and higher initial concentration of calcium. The results of XRD analysis (Villar et al., 2008b) show a slight decrease in the calcite content in the 92 months test. A comparison between the *post-mortem analysis* results against the experimental results for the dissolved bicarbonate concentration is presented in Figure 9. A close agreement in terms of distribution pattern for all time intervals can be highlighted. The concentration of bicarbonate shows an increase in the hydration side that is consistent with experimental observations. This is anticipated to be attributed to the localised dissolution of calcite in the hydration end (Figure 7). The results indicate that the calcite dissolution has occurred in a region of about 100 mm close to the hydration side. In this region a lower amount of calcium and high amount of bicarbonate existed prior to the *post-mortem analyses*. As a result, calcite is dissolved to maintain the equilibrium condition. The reduced bicarbonate content can be correlated to dissolution of calcite at the heating boundary as also noted by Fernández and Villar (2010).

5.3. Chemical behaviour - Cationic species and pH

Figures 11 present the results of numerical simulation for the dissolved cationic species including sodium (Na^+), calcium (Ca^{2+}), magnesium (Mg^{2+}) and potassium (K^+) in the domain, respectively. Similar distribution patterns for the cationic species are observed. The concentrations of cationic species are observed to be reduced in the vicinity of hydration side due to the advection process. The ions flushed through the sample have been accumulated in the first half of the domain away from the hydration side. Cationic species have been transferred by the advection and diffusion towards the

heater, providing areas with greater concentrations than the initial value within a length that ranges between 50 mm to 350 mm away from the hydration source. The increased concentrations of cations close to the heater and their reduction in the areas approximately between 50 and 300 mm away from the heater are controlled by the simultaneous water and vapour flow in the area within the 300mm distance from the heater.

The transport processes of sodium ions were only affected by the ion exchange reaction as the sodium ions were not involved in any mineral precipitation and dissolution reactions. Figure 12 presents the variations of exchangeable sodium in the domain obtained from the numerical analysis. Except for limited regions close to the boundaries small variations from the initial amount of the exchangeable sodium can be observed. The evolution of the exchangeable sodium is driven mainly by the excess amount of calcium in the vicinity of heater which resulted to the replacement of the sodium ions by calcium ions in the interlayer. On the other hand, the calcium concentration was reduced in the solution in the distance of 20 to 300 mm, providing the conditions for the replacement of calcium by sodium ions in the interlayer. The distribution of the dissolved calcium in the domain was affected by the presence and evolution of the mineral reactions (anhydrite, gypsum and calcite) and ion exchange reactions. The effects of mineral reaction are mainly related to the dissolution of gypsum and precipitation of anhydrite than calcite.

From Figure 11, it can be observed that the concentration of magnesium decreased by the advection and increases in the first 250 mm away from the injection point. It is noted that only ion exchange have been involved as a chemical reaction that involves magnesium in the numerical analysis. Dissolution/precipitation of dolomite was not considered and that may cause some level of uncertainty about the fate of magnesium. However, it is anticipated that the transport processes had a greater contribution in the evolution of magnesium. As shown in Figure 12, limited variation of the exchangeable magnesium in the domain has occurred, except in the region affected by the elevated temperature. The pore fluid in this region contained larger amount of sodium and magnesium than that of calcium due to the precipitation of anhydrite. This resulted in the replacement of calcium exchangeable ions with sodium and magnesium.

Figure 11 also shows the distribution profiles of potassium in the domain. The behaviour is more similar to those observed for sodium and magnesium than that of calcium. From Figure 12, it can be observed that potassium exchangeable ions were replaced by sodium and magnesium ions in the interlayer in the region close to the heater. It is noted that only ion exchange reactions have geochemically affected the distribution of potassium.

The results of *post-mortem analysis* and the experimental data for the dissolved sodium are presented in Figure 13. The overall trend of distribution is in agreement with the experimental results for all time intervals. In the area close to the heater, a higher concentration of sodium ions is observed from the numerical analysis than those reported from the experiments. This can be explained by the higher drying predicted by the model for the periods of 6, 12, 24 months at this region. Elevated temperature has controlled the dissolution of anhydrite and precipitation of anhydrite in the vicinity of heater alongside transport processes. The behaviour of calcium is governed by combined effects of advection-diffusion of excess ions and geochemical reactions. The distribution of magnesium (Figure 13) shows a reduced concentration in areas close to the hydration. The concentration of magnesium was increased close to the heater and reduced in the area between about 50 to 300 mm from the heater that is qualitatively in agreement with the experimental result. The increase in magnesium content observed in the experimental tests is described to be influenced by temperature (near the heater) and the advance of the water front along the bentonite column (Fernández and Villar, 2010). Fernández and Villar (2010) reported that for all tests, there was an increase in the soluble Mg^{2+} , Na^+ , K^+ and Ca^{2+} concentrations close to the heater, whereas the K^+ content decreased near the hydration source and Na^+ decreased in that region. From Figure 13, it can be observed that the amount of potassium has been reduced in a limited area close to the hydration. The potassium ions transferred by water have been added in the first half of the domain at the hydration side. A high amount of potassium was precipitated due to water-vapour advection process in the 300 mm distance for the heater that is similar to the behaviour of other cations.

As shown in Figure 12, the exchangeable composition of ions shows higher amount of sodium and magnesium from the initial state close to the heater. The concentration of calcium and potassium ions

in the exchangeable composition is reduced that is governed by the precipitation of anhydrite and dissolution of gypsum at the hot boundary region. This is also compatible with observation of the pore fluid composition in this region that contains high concentrations of sodium and magnesium than calcium. The potassium exchangeable ions have been also replaced by sodium and magnesium ions to a lesser extent, providing a new equilibrium condition in the exchangeable composition.

The results of pH variation of the soil water system from the transient numerical simulation are presented in Figure 14. The variation of H^+ ions (and pH) is governed only by the geochemical reactions in the transient numerical analysis as H^+ was not considered in the transport analysis. The pH was calculated in the charge balance of geochemical analysis by PHREEQC (Parkhurst and Appelo, 1999). The variation of pH in the domain shows a similar pattern to that presented for the bicarbonate in the hydration zone. As shown in Figure 9, a high amount of bicarbonate has been accumulated in the hydration affected zone. The pH decreases from the initial value in the domain from 200 mm to approximately 500 mm away from the hydration side and increases over the 92 months of the analysis. The pH decrease in this region can be explained by the dissolution of gypsum and accumulation of sulfate in the soil water. An increase in pH is observed in the vicinity of heater for up to approximately 100 mm distance from the heating boundary. This is related to the precipitation of anhydrite where the gypsum content was reduced.

Figure 14 shows the results of post-mortem modelling of pH and provides a comparison between the numerical prediction against the experimental results reported by Fernández and Villar (2010). The experimental results reported were only available for the 92 months analysis. The pH evolution shows limited increase in the hydration side and decrease in the area close to the heating boundary. The behaviour exhibits similar trend to that observed for bicarbonate. The results are in qualitative agreement with the overall observed in the experiment. The decrease in pH in the heater side can be attributed to the precipitation of calcite. The calcite dissolution has similarly governed the increase in pH in the hydration side. As shown in Figure 14, the results of post mortem analysis for pH for the 92 months duration are generally higher than those reported by Fernández and Villar (2010). This is related to the difference between the initial pH value used in the numerical simulation and that of the

experiment reported by Fernández and Villar (2010). The initial pH used in the numerical analysis (i.e. pH=8.60) was calculated from the geochemical pore water simulation (Table 2) that is in close agreement the experimental value reported by Fernández et al. (2004) (i.e. pH=8.73). It is noted that the pH of FEBEX bentonite reported at the same solid/water ration reported by ENRESA (2000) is lower (i.e. pH=7.93). The difference can be related to variations of the FEBEX material and its constituents used in ENRESA (2000) and Fernández et al. (2004).

6) Conclusions

The analysis of coupled thermal, hydraulic and chemical behaviour of compacted bentonite presented here highlights key geochemical reactions involved under the heating and hydration conditions imposed to the compacted bentonite buffer. Using the experimental results of up to 92 months the validity of the theoretical formulations and numerical model developed under the conditions of the problem studied has been examined. The results indicated that temperature variation in the system has reached steady-state conditions within a considerably shorter time compared with the hydraulic and chemical processes.

The impacts of the interlayer water on the hydraulic flow behaviour were considered via the interlayer hydration model that addresses the major effect of microstructure swelling/shrinkage on the flow behaviour. The model also showed a close correlation with respect to the saturation period of the FEBEX bentonite by using the proposed unsaturated hydraulic conductivity. Elevated temperature in the heater side showed a profound effect on the distribution of ions and minerals. Higher flow of water and vaporisation is likely to have occurred in the system, facilitating the migration of major ionic species towards the heater by advection mechanism.

The simulation results of the chloride ions showed a good qualitative agreement with the experimental results especially for the periods of 6, 12 and 24 months. The lower chloride concentration from numerical simulation compared to those reported in the experiment indicates that further processes can be involved that control the flow regime of moisture in the system in the areas affected by the temperature (where the cycle of evaporation-condensation mainly controlled the distribution of

chloride). Long term results (92 months) highlights that further development on the hydraulic conductivity model or inclusion of thermally coupled processes are required. The accessory minerals in FEBEX bentonite such as gypsum and carbonates (despite the small proportion in the composition) showed considerable effects on the distribution of anionic species. The fate of cationic species was found to be mainly controlled by the transport processes. The model showed compatible trends in comparison with the pore fluid composition observed with the available experimental dataset. Gypsum was found to be dissolved in the area close to the heating boundary, producing considerable amount of dissolved sulfate. The composition of exchangeable ions remained the same as the initial condition except mainly for limited distances from the heater based on the transient simulation results. This indicates the possibility of conversion of FEBEX bentonite from Ca/Mg-smectite clay to Na/Mg smectite. The consequence in long term can affect the swelling pressure predicted for the clay buffer. The research presented provide further insights into the hydro-geochemically coupled processes in compacted bentonite buffer and its evolution under the thermal and hydraulic conditions of the geological disposal for high level radioactive waste.

Acknowledgment

The financial support received by the first author in the form of a PhD scholarship from the UK's Overseas Research Students Awards Scheme (ORSAS) is gratefully acknowledged. The support and contribution from Dr Suresh C. Seetharam (former Research Fellow at Cardiff University and currently a Scientist at the Belgian Nuclear Research Centre) in the early stages of this research is also gratefully acknowledged.

Appendix A

The mass conservation equation for the i^{th} chemical component in multi-ionic system of unsaturated porous media can be written in a general form as:

$$\frac{\partial(\theta_l c_i \delta V)}{\partial t} + \frac{\partial(\theta_l s_i \delta V)}{\partial t} + \delta V \nabla \cdot J_i = 0 \quad (A1)$$

where, J_i is the total chemical flux accounting for the sum of advective, diffusive and dispersive fluxes.

An aqueous solution is electrically neutral on macroscopic scale and the charge should remained balanced (Lasaga, 1979). The general form of charge conservation on the transport processes can be given as (Sedighi et al. 2011):

$$\sum_{i=1}^{n_c} \frac{\partial(\theta_l F z_i c_i \delta V)}{\partial t} + \sum_{i=1}^{n_c} \frac{\partial(\theta_l F z_i s_i \delta V)}{\partial t} + \sum_{i=1}^{n_c} \delta V \nabla \cdot F z_i J_i = 0 \quad (A2)$$

where, F is Faraday constant.

Assuming that the charge is separately conserved in geochemical reactions, (i.e. $\sum_{i=1}^{n_c} \frac{\partial(\theta_l z_i s_i \delta V)}{\partial t} = 0$), the electro-neutrality for the transport part can be divided into two separate requirements (e.g. Lasaga, 1979): i) the total charge should be conserved (i.e. no net charge $\sum_{i=1}^{n_c} \frac{\partial(\theta_l z_i c_i \delta V)}{\partial t} = 0$) and ii) no electrical current should run through the solution (i.e. no current condition $\sum_{i=1}^{n_c} \delta V \nabla \cdot (z_i J_i) = 0$).

Sedighi et al. (2011) and Thomas et al. (2012) have proposed a general formulation for the diffusive flux in aqueous solution due to concentration potential, electrical potential and thermal potential by expanding the formulations proposed by Lasaga (1979) for multicomponent chemical diffusion and the heat of transport by Ballufi et al. (2005), given as:

$$J_i^{diff} = -\frac{D_i^0 c_i}{RT} \frac{\partial \mu_i}{\partial c_i} \nabla c_i - \frac{D_i^0 F z_i c_i}{RT} \nabla \Phi - \frac{D_i^0 c_i Q_i^*}{RT^2} \nabla T \quad (A3)$$

where μ_i is the chemical potential of the i^{th} component, Φ is the electrical potential and Q_i^* represents the heat of transport of the i^{th} component.

The gradient of electrical potential can therefore be determined explicitly by considering “no current condition” ($\sum_{j=1}^{n_c} \delta V \nabla \cdot (z_j J_j) = 0$):

$$\nabla\Phi = -\frac{1}{F} \left[\frac{\sum_{j=1}^{n_c} D_j^0 z_j c_j \frac{\partial \mu_j}{\partial c_j} \nabla c_j + \sum_{j=1}^{n_c} D_j^0 z_j c_j \frac{Q_i^*}{T} \nabla T}{\sum_{j=1}^{n_c} D_j^0 z_j^2 c_j} \right] \quad (\text{A4})$$

731 The derivative of chemical potential with respect to concentration is (Oelkers, 1996):

$$\frac{\partial \mu_j}{\partial c_j} = -\frac{RT}{c_j} \left[1 + \frac{\partial \ln \gamma_i}{\partial c_i} \right] \quad (\text{A5})$$

732 Substituting the electrical potential from equation (A5) into equation (A3) yields:

$$\begin{aligned} J_i^{diff} = & -D_i^0 \left(1 + \frac{\partial \ln \gamma_i}{\partial c_i} \right) \nabla c_i + \frac{D_i^0 z_i c_i}{\sum_{z=1}^{n_c} D_z^0 z_z^2 c_z} \sum_{j=1}^{n_c} D_j^0 z_j \left(1 + \frac{\partial \ln \gamma_i}{\partial c_i} \right) \nabla c_j - \frac{D_i^0 c_i Q_i^*}{RT^2} \nabla T \\ & + \frac{D_i^0 z_i c_i}{\sum_{z=1}^{n_c} D_z^0 z_z^2 c_z} \sum_{j=1}^{n_c} D_j^0 z_j c_j \frac{Q_j^*}{RT^2} \nabla T \end{aligned} \quad (\text{A6})$$

733 The total flux of due to dvection, diffusion and dispersion can be implemented in the mass
734 conservation that yields:

$$\frac{\partial(\theta_l c_i \delta V)}{\partial t} + \frac{\partial(\theta_l s_i \delta V)}{\partial t} = -\delta V \nabla \cdot \left(c_i \mathbf{v}_l - \sum_{j=1}^{n_c} \theta_l \tau_i D_{ij} \nabla c_j - \theta_l \tau_i D_i^T \nabla T - \mathbf{D}_m \nabla c_j \right) \quad (\text{A7})$$

735 The overall charge is conserved by implementing the “no charge” and “no current” conditions. In
736 addition, the electro-neutrality must be maintained in geochemical reactions model too. The charge
737 conservation in the reactions is adjusted by the pH in the solution in PHREEQC (Parkhurst and
738 Appelo, 1999). The advective and dispersive fluxes are not considered in the “no current” condition
739 (all ions move with the same rate). If the overall charge conservation equation is explicitly employed
740 in combination with the n_c conservation equations for mass, an over-determined system of equations
741 is obtained (Lasaga, 1979 and Boudreau et al., 2004). As proposed by Lasaga (1979), one of the
742 concentrations and its derivatives needs to be eliminated from all the equations. A particular
743 dependent ion is therefore eliminated from the model whilst its concentration is calculated from
744 $(n_c - 1)$ components by the charge conservation equation (Lasaga 1981; Boudreau et al. 2004). In

other words, the mass conservation is solved for $(n_c - 1)$ components where the diffusive flux does no longer contain the mutual dependant concentration effects. Accordingly, a *dependent ion* is removed from the mass conservation in the transport model and its actual concentration is calculated by knowing the concentration of the remained $(n_c - 1)$ components through the no-charge condition $\sum_{i=1}^{n_c} \frac{\partial(\theta_l z_i c_i \delta V)}{\partial t} = 0$.

Appendix B:

The governing differential equation for transport of an arbitrary chemical component in a coupled form with thermal, hydraulic and chemical primary variable can be described as:

$$C_{c_{il}} \frac{\partial u_l}{\partial t} + C_{c_{iT}} \frac{\partial T}{\partial t} + C_{c_{ia}} \frac{\partial u_a}{\partial t} + C_{c_i} \frac{\partial c_i}{\partial t} = \nabla \cdot (K_{c_{il}} \nabla u_l) + \nabla \cdot (K_{c_{iT}} \nabla T) + \nabla \cdot (K_{c_{ia}} \nabla u_a) + \nabla \cdot \left(\sum_{j=1}^{n_c} K_{c_{ij}} \nabla c_j \right) + f_{c_i} \quad (B1)$$

where C and K are lumped coefficients of the equation. f_{c_i} represents the chemical flux of the i^{th} component normal to the boundary surface.

The numerical solution of the formulations is achieved by the application of the finite element (in space) and the finite difference (in time) (Thomas and He, 1998). The Galerkin weighted residual method is adopted by which the special discretisation is developed and the residual error resulting from an approximate function over the entire element domain is minimised using the shape functions, given as:

$$\int N_r R_{\Omega} d\Omega^e = 0 \quad (B2)$$

where, N_r is the shape function, R_{Ω} is the residual factor and Ω^e represents the entire element domain.

Applying this method to the governing differential equation for an arbitrary chemical component in terms of the approximate functions yields:

$$\int N_r \left[-C_{c_i l} \frac{\partial u_l}{\partial t} - C_{c_i T} \frac{\partial T}{\partial t} - C_{c_i a} \frac{\partial u_a}{\partial t} - C_{c_i} \frac{\partial c_i}{\partial t} + \nabla \cdot (K_{c_i T} \nabla T) + \nabla \cdot (K_{c_i a} \nabla u_a) + \nabla \cdot \left(\sum_{j=1}^{n_c} K_{c_i c_j} \nabla c_j \right) + J_{c_i} \right] d\Omega^e = 0 \quad (\text{B3})$$

763 The spatially discretised equations can then be combined and presented in a matrix form: (Thomas
764 and He, 1998):

$$\mathbf{K}\{\phi\} + \mathbf{C}\left\{\frac{\partial \phi}{\partial t}\right\} = \{f\} \quad (\text{B4})$$

765 where ϕ is the vector of primary variables (unknowns). \mathbf{K} , \mathbf{C} are the corresponding matrices of the
766 governing equation. f is the RHS vector and detailed elsewhere (Seetharam et al., 2007).

767 Details of the numerical solution to the coupled THM and THCM formulation of the model have been
768 comprehensively discussed by (Thomas and He, 1998; Seetharam et al., 2007).

769 The computational solution used for the reactive transport formulations is based on a time-splitting
770 approach. The governing equations for the transport and the geochemical reactions are therefore
771 solved sequentially. The coupling scheme adopted here between the transport model (COMPASS) and
772 geochemical model (PHREEQC) is a sequential non-iterative approach (SNIA). Figure (B1) presents
773 the SNIA coupling approach and modular data exchange between COMPASS and PHREEQC.

774 The numerical formulation concerning reactive chemical equations by PHREEQC has been described
775 elsewhere (Parkhurst and Appelo, 1999). The model has been used with no alteration to its numerical
776 formulation. In summary, there are two numerical solutions adopted in PHREEQC to solve problems
777 involved multiple chemical reactions (Parkhurst and Appelo, 1999):

778 i) A modified *Newton-Raphson method* is employed to solve a series of non-linear algebraic equations
779 for chemical reactions under equilibrium reactions.

ii) For kinetically controlled reaction, the model uses a *Runge-Kutta algorithm*, which integrates the rate of reactions over time. The scheme includes a Runge-Kutta method with lower order to derive an error estimate with up to six intermediate evaluations of the derivative (Parkhurst and Appelo, 1999).

References

Agar, J.N., Mou, C.Y., and Lin, J. 1989. Single-ion heat of transport in electrolyte solutions, A hydrodynamic theory. *Journal of Physical Chemistry*, 93, 2079-2082.

Arcos, D., Grandia, F., Domènech, C., Fernández, A.M., Villar, M.V., Muurinen, A., Carlsson, T., Sellin, P., and Hernán, P. 2008. Long-term geochemical evolution of the near field repository: Insights from reactive transport modelling and experimental evidences. *Journal of Contaminant Hydrology*, 102 (3-4), 196-209.

Boudreau, B.P., Meysman, F.J.R. and Middelburg, J.J. 2004. Multicomponent ionic diffusion in pore water: Columbic effects revisited. *Earth Planetary Science Letters*, 222, 653-666.

Cleall, P.J., Seetharam, S.C., and Thomas, H.R. 2007. On the inclusion of some aspects of chemical behaviour of an unsaturated soil in thermo-hydro-chemical-mechanical models: II: Application and transport of soluble salts in compacted bentonite. *Journal of Engineering Mechanics*, ASCE, 133, 348-356.

Cuevas, J., Villar, M.V., Martín, M., Cobeña, J.C., and Leguey, S. 2002. Thermo-hydraulic gradients on bentonite: distribution of soluble salts, microstructure and modification of the hydraulic and mechanical behaviour. *Applied Clay Science*, 22, 25-38.

Cussler, E.L. 1997. *Diffusion-Mass Transfer in Fluid Systems*. University Press, Cambridge.

ENRESA. 2000. *Full-scale engineered barriers experiment for a deep geological repository for high-level radioactive waste in crystalline host rock*. FEBEX project. EUR 19147, Nuclear Science and Technology Series, European Communities, Luxembourg.

Fernández, A.M., Cuevas, J., and Rivas, P. 2001. *Pore water chemistry of the FEBEX bentonite*. Material Research Society Symposium Proceeding. 663, 573-588.

805 Fernández, A.M., and Villar, M.V. 2010. Geochemical behaviour of a bentonite barrier in the
 806 laboratory after up to 8 years of heating and hydration. *Applied Geochemistry*, 25, 809-824.

807 García-Gutiérrez, M., Cormenzana, J.L., Missana, T., and Mingarro, M. 2004. Diffusion coefficients
 808 and accessible porosity for HTO and ³⁶Cl in compacted FEBEX bentonite. *Applied Clay Science*, 26,
 809 65-73.

810 Guimarães, L.D.N., Gens, A., and Olivella, S. 2007. Coupled thermo-hydro-mechanical and chemical
 811 analysis of expansive clay subjected to heating and hydration. *Transport in Porous Media*, 66, 341-
 812 372.

813 Holmboe, M., Wold, S., Jonsson, M., 2012. Porosity investigation of compacted bentonite using XRD
 814 profile modelling. *Journal of Contaminant Hydrology*. 128, 19–32.

815 Hueckel, T.A. 1992. Water-mineral interaction in hydromechanics of clay exposed to environmental
 816 loads: a mixture-theory approach. *Canadian Geotechnical Journal*, 29, 1071-1086.

817 Jacques, D., and J. Šimůnek. 2005. *User manual of the Multicomponent Variably- Saturated Flow and*
 818 *Transport Model HPI. Description, verification, and examples. Version 1.0.* BLG-998 Report
 819 SCK·CEN, Mol, Belgium.

820 Kozaki, T., Inada, K., Sato, S., and Ohashi, H. 2001. Diffusion mechanism of chloride ions in sodium
 821 montmorillonite. *Journal of Contaminant Hydrology*, 47, 159-170.

822 Kröhn, K-P. 2003. New conceptual models for the resaturation of bentonite. *Applied Clay Science*, 23,
 823 25-33.

824 Laird, D.A. 2006. Influence of layer charge on swelling of smectite. *Applied Clay Science*, 34, 74-87.

825 Langmuir, D. 1997. *Aqueous Environmental Geochemistry*. Prentice Hall.

826 Lasaga, A.C. 1979. The treatment of multicomponent diffusion and ion pairs in diagenetic fluxes.
 827 *American Journal of Science*, 279, 324-346.

828 Lasaga, A.C. 1998. *Kinetic Theory in the Earth Science*. Princeton Series in Geochemistry, Princeton
 829 University Press.

830 Likos, W.J., and Lu, N. 2006. Pore-scale analysis of bulk volume change from crystalline swelling in
831 Na^+ and Ca^{2+} smectite. *Clays and Clay Minerals*, 54, 516-529.

832 Likos, W.J., and Wayllace, A. 2010. Porosity evolution of free and confined bentonite during
833 interlayer hydration, *Clays and Clay Minerals*, 58, 399-414.

834 Martín, M., Cuevas, J., and Leguey, S. 2000. Diffusion of soluble salts under a temperature gradient
835 after the hydration of compacted bentonite. *Applied Clay Science*, 17, 55-70.

836 Mayhew, Y.R., and Rogers, G.F.C. 1976. *Thermodynamic and transport properties of fluids*. 2nd
837 edition, Oxford, Blackwell.

838 Muurinen, A., Karnland, O., and Lehikoinen, J. 2007. Effect of homogenization on the microstructure
839 and exclusion of chloride in compacted bentonite. *Physics and Chemistry of the Earth*, 32, 485-490.

840 Navarro, V, Asensio, L, Yustres, Á, Pintado, X and Alonso, J. 2014. An elastoplastic model of
841 bentonite free swelling. *Engineering Geology*, 181, 190-201.

842 Oelkers, E. 1996. *Physical and chemical properties of rocks and fluids form chemical mass transport*
843 *calculations*. Reactive Transport in Porous Media, Reviews in Mineralogy, 34, 130-191.

844 Parkhurst, D.L., and Appelo, C.A.J. 1999. *User's guide to PHREEQC (version 2)*. U.S. Geological
845 Survey, Water Resource Investigation Report, 99-4259.

846 Philip, J.R., and de Vries, D.A. 1957. Moisture movement in porous materials under temperature
847 gradients. *Transaction American Geophysical Union*, 38(2), 222-232.

848 Pusch, R., Yong, R.N., 2006. *Microstructure of Smectite Clays and Engineering Performance*. Taylor
849 and Francis, New York.

850 Pusch, R., Karnland, O., and Hokmark, H. 1990. *GMM: a general microstructural model for*
851 *qualitative and quantitative studies of smectite clays*, SKB, Technical Report, SKB-90-43, Stockholm.

852 Ransom, B. and Helgeson, H.C. 1994. A chemical and thermodynamic model of aluminous
853 dioctahedral 2:1 layer clay minerals in diagenetic processes: Regular solution representation of
854 interlayer dehydration in smectite. *American Journal of Science*, 294, 449-484.

855 Ransom, B., and Helgeson, H.C. 1995. A chemical and thermodynamic model of aluminous
856 dioctahedral 2:1 layer clay minerals in diagenetic processes: Dehydration of dioctahedral aluminous
857 smectites as a function of temperature and depth in sedimentary, *American Journal of Science*, 295,
858 245-281.

859 Revil, A., and Jougnot, D. 2008. Diffusion of ions in unsaturated porous materials. *Journal of Colloid*
860 *and Interface Science*. 319, 226-235.

861 Samper, J., Zheng, L., Montenegro, L., Fernández, A.M., and Rivas, P. 2008. Testing coupled thermo-
862 hydro-chemical models of compacted bentonite after dismantling the FEBEX in situ test. *Applied*
863 *Geochemistry*, 23(5), 1186-1201.

864 Samper, J., Xu, T., and Yang, C. 2009. A sequential partly iterative approach for multicomponent
865 reactive transport with CORE2D. *Computers and Geosciences*, 13, 301-316.

866 Sánchez, M., Gens, A., Olivella, S. 2012. THM analysis of a large-scale heating test incorporating
867 material fabric changes. *International Journal of Numerical and Analytical Methods in Geomechanics*.
868 36, 391-421.

869 Sedighi, M., 2011. *An investigation of hydro-geochemical processes in coupled thermal, hydraulic,*
870 *chemical and mechanical behaviour of unsaturated soils*. Ph.D. Thesis Cardiff University, UK.
871 (<http://orca.cf.ac.uk/54236/1/U573143.pdf>).

872 Sedighi, M., and Thomas, H.R. 2014. Micro porosity evolution in compacted swelling clays- A
873 chemical approach. *Applied Clay Science*, 101, 608-618.

874 Sedighi, M., Thomas H.R., Vardon P.J. 2011. *Modelling thermal impacts on reactive transport*
875 *processes related to multicomponent chemicals in compacted clays*. In Proceedings of the 2nd
876 International Symposium on Computational Geomechanics (ComGeo II), Cavtat-Dubrovnik, 538-546.

877 Sedighi, M., Thomas, H.R., Masum, S.A., Vardon, P.J., Nicholson, D., and Chen, Q. 2015.
878 Geochemical modelling of hydrogen gas migration in an unsaturated bentonite buffer. *Geological*
879 *Society Journal*, 415, 189-201.

880 Sedighi, M., Thomas, H. R., and Vardon, P. J. 2016. Reactive transport of chemicals in unsaturated
881 soils: Numerical model development and verification. *Canadian Geotechnical Journal*, 52, 1–11.

882 Seetharam, S.C., Thomas, H.R., and Cleall, P.J. 2007. Coupled thermo-hydrochemical- mechanical
883 model for unsaturated soils-numerical algorithm. *International Journal of Numerical Methods in*
884 *Engineering*, 70: 1480-1511.

885 Steefel, C.I., and MacQuarrie, K.T.B. 1996. *Approaches to modeling of reactive transport in porous*
886 *media*. Reactive Transport in Porous Media, Reviews in Mineralogy, (34). Mineralogical Society of
887 America, Washington, DC.

888 Steefel, C.I. and Sergi, M. 2016. *CrunchFlow Software for Modeling Multicomponent Reactive Flow*
889 *and Transport, User's Manual*. Lawrence Berkeley National Laboratory.
890 <http://www.csteefel.com/CrunchFlowManual.pdf>.

891 Steefel, C.I., Rutqvist, J. Tsang, C-F., Liu, H-H., Sonnenthal, E., Houseworth J., and Birkholzer, J.
892 2010. *Reactive Transport and Coupled THM Processes in Engineering Barrier Systems (EBS)*.
893 Technical Report, LBNL-3901E, Lawrence Berkeley National Laboratory.

894 Thomas, H. R., and He, Y. 1997. A coupled heat–moisture transfer theory for deformable unsaturated
895 soil and its algorithmic implementation. *International Journal of Numerical Methods in Engineering*,
896 40(18), 3421-3441.

897 Thomas, H.R., Cleall, P.J., Chandler, N., Dixon, D. and Mitchell, H.P. 2003. Water infiltration into a
898 large-scale in-situ experiment in an underground research laboratory. *Géotechnique*, 53 (2), 207–224.

899 Thomas, H.R., Sedighi, M., 2012. Modelling the Engineering Behaviour of Highly Swelling Clays.
900 Keynote Paper, *In Proceeding of the 4th International Conference on Problematic Soils*, Wuhan,
901 China, 21-33.

902 Thomas, H.R., Sedighi, M., and Vardon, P.J. 2012. Diffusive reactive transport of multicomponent
903 chemicals under coupled thermal, hydraulic, chemical and mechanical conditions. *Geotechnical and*
904 *Geological Engineering*, 30(4): 841– 857.

905 van Genuchten, M.Th. 1980. A closed-form equation for predicting the hydraulic conductivity of
 906 unsaturated soils. *Soil Science Society of America Journal*, 44, 892-898.

907 Van Loon, L.R., Glaus, M.A., and Müller, W. 2007. Anion exclusion effects in compacted bentonite:
 908 Towards a better understanding of anion diffusion. *Applied Geochemistry*, 22, 2536-2552.

909 Vardon P.J., Cleall P.J., Thomas, H.R., Philp, R.N. and Banicescu, I. 2011. Three-dimensional field-
 910 scale coupled thermo-hydro-mechanical modelling: a parallel computing implementation. *ASCE*
 911 *International Journal of Geomechanics*, 11(2), 90-99.

912 Vidal, O., and Dubacq, B. 2009. Thermodynamic modelling of clay dehydration, stability and
 913 compositional evolution with temperature, pressure and H₂O activity. *Geochimica et Cosmochimica*
 914 *Acta*, 73(21), 6544-6564.

915 Villar, M.V. 2007. Water retention of two natural compacted bentonites. *Clays and Clay Minerals*,
 916 55(3), 311-322.

917 Villar, M.V., Fernández, A.M., Martín, P.L., Barcala, J.M., Gómez-Espina, R., and Rivas, P. 2008a.
 918 *Effect of Heating/Hydration on Compacted Bentonite: Tests in 60 cm Long Cells*. Publishing House
 919 CIEMAT. Madrid. ISBN: 978-84-7834-597-4.

920 Villar, M.V., Sánchez, M., and Gens, A. 2008b. Behaviour of a bentonite barrier in the laboratory:
 921 experimental results up to 8 years and numerical simulation. *Physics and Chemistry of the Earth*, 33,
 922 S476-S485.

923 Warr, L., Berger, J., 2007. Hydration of bentonite in natural waters: application of “confined volume”
 924 wet-cell X-ray diffractometry. *Physic and Chemistry of Earth A/B/C*, 32 (1–7), 247–258

925 Wersin, P., Curti, E., and Appelo, C.A.J. 2004. Modelling bentonite-water interaction at high
 926 solid/liquid ratios: swelling and diffuse double layer effects. *Applied Clay Science*, 26, 249-257.

927 Xie, M., Bauer, S., Kolditz, O., Nowak, T., and Shao, H. 2006. Numerical simulation of reactive
 928 processes in an experiment with partially saturated bentonite, *Journal of Contaminant Hydrology*, 83,
 929 122-47.

930 Xu, T., Samper, J., Ayora, C., Manzano, M., and Emilio, C. 1999. Modeling of non-isothermal multi-
 931 component reactive transport in field scale porous media flow systems. *Journal of Hydrology*, 214,
 932 144-164.

933 Yang, C., Samper, J., and Montenegro, L. 2008. A coupled non-isothermal reactive transport model
 934 for long-term geochemical evolution of a HLW repository in clay. *Environmental Geology*, 53(8),
 935 1627-1638.

936 Yeh, G.T., and Tripathi, V.S. 1989. A critical evaluation of recent developments in hydrogeochemical
 937 transport models of reactive multichemical components. *Water Resources Research*, 25(1), 93-108.

938 Yong, R.N. 2003. Influence of microstructural features on water, ion diffusion and transport in clay
 939 soils. *Applied Clay Science*, 23, 3-13.

940 Zagorščak, R., Sedighi, M., and Thomas, H.R. 2017. Effects of thermo-osmosis on hydraulic behavior
 941 of saturated clays. *ASCE International Journal of Geomechanics*. 17(3),
 942 [http://dx.doi.org/10.1061/\(ASCE\)GM.1943-5622.0000742](http://dx.doi.org/10.1061/(ASCE)GM.1943-5622.0000742).

943 Zheng, L. and J. Samper, 2008, Coupled THMC model of FEBEX mock-up test, *Physics and*
 944 *Chemistry of the Earth, Physics and Chemistry of the Earth*, 33, 486-98.

945

946

947 List of Tables

948 **Table 1.** Thermodynamic parameters used for dissolution/precipitation of minerals (adopted from the
949 phreeqc.dat database by Pankhurst and Appelo, 1999) and the equilibrium constants of the ion
950 exchange reactions for the FEBEX bentonite (adopted from Fernández et al. 2001).

951 **Table 2.** Initial geochemistry of the clay-water system and injected aqueous solution.

952 **Table 3.** Thermal and hydraulic properties and relationships.

953 **Table 4.** Parameters used in the hydration/dehydration model for the FEBEX bentonite in order to
954 calculate the interlayer hydrate water content.

955

956 List of Figures

957 **Fig.1.** Schematic of the heating and hydration experiments reported by Villar et al., (2008).

958 **Fig.2.** The initial and boundary conditions applied for coupled thermal, hydraulic and chemical
959 simulation of the heating and hydration experiments.

960 **Fig.3.** Schematic of the “micro porosity” and “macro porosity” definition in compacted smectite clay.

961 **Fig.4.** Variations of temperature in the domain obtained from the *transient analysis*
962 (lines) and experiments (Villar et al., 2008b) (symbols).

963 **Fig.5.** Variations of degree of saturation in the domain obtained from the *transient analysis* (symbols)
964 and experiments (calculated from data by Villar et al., 2008b) (lines).

965 **Fig. 6.** Variations of chloride in the domain obtained from the *transient analysis* (lines) and
966 experimental results (Fernández and Villar, 2010) (symbols).

967 **Fig. 7.** Variations of sulfate in the domain obtained from the *transient analysis* (left) and *post-mortem*
968 (right) analysis. Experimental results (symbols) are from Fernández and Villar (2010).

969 **Fig.8.** Variations of gypsum (left) and anhydrite (right) in the domain obtained from the *transient*
970 *analysis*.

971 **Fig.9.** Variations of bicarbonate in the domain obtained from the *transient analysis* (left) and *post-*
972 *mortem* (right) analysis. Experimental results (symbols) are from Fernández and Villar (2010).

973 **Fig.10.** Variations of calcite in the domain obtained from the *transient analysis*.

974 **Fig.11.** Variations of cationic ions in the domain obtained from the *transient analysis*.

975 **Fig.12.** Variations of exchangeable ions in the domain obtained from *transient analysis*.

976 **Fig.13.** Variations of cationic ions in the domain obtained from the *post mortem analysis* (lines) and
977 experiments (Fernández and Villar, 2010) (symbols).

978 **Fig.14.** Variations of pH in the domain obtained from obtained i) from *transient analysis* (left) and ii)
979 the *post mortem analysis* (left) where and experiments (Fernández and Villar, 2010) are also
980 presented (symbols).

981 **Fig.B1.** The sequential non-iterative approach (SNIA) adopted for coupling the transport model
982 (COMPASS) and geochemical model (PHREEQC).

983

Table 1. Thermodynamic parameters used for dissolution/precipitation of minerals (adopted from the phreeqc.dat database by Pankhurst and Appelo, 1999) and the equilibrium constants of the ion exchange reactions for the FEBEX bentonite (adopted from Fernández et al. 2001).

| Reactions | Thermodynamic parameters | |
|--|--------------------------|-----------------------|
| | $\log K_{eq}$ (25 °C) | ΔH_r^0 (kcal) |
| Mineral dissolution/precipitation: | | |
| $\text{CaSO}_4 = \text{Ca}^{2+} + \text{SO}_4^{2-}$ (Anhydrite) | -4.360 | -1.710 |
| $\text{CaSO}_4 \cdot 2\text{H}_2\text{O} = \text{Ca}^{2+} + \text{SO}_4^{2-} + 2\text{H}_2\text{O}$ (Gypsum) | -4.580 | -0.109 |
| $\text{NaCl} = \text{Na}^+ + \text{Cl}^-$ (Halite) | 1.582 | 0.918 |
| $\text{CaCO}_3 = \text{Ca}^{2+} + \text{CO}_3^{2-}$ (Carbonate) | -8.480 | -2.297 |
| Ion exchange: | | |
| $\text{Na-X} = \text{Na}^+ + \text{X}^-$ | 0.0 | - |
| $\text{Ca-X}_2 = \text{Ca}^{2+} + 2\text{X}^-$ | 0.774 | - |
| $\text{Mg-X}_2 = \text{Mg}^{2+} + 2\text{X}^-$ | 0.655 | - |
| $\text{K-X} = \text{K}^+ + \text{X}^-$ | 0.878 | - |

Table 2. Initial geochemistry of the clay-water system and injected aqueous solution

| Pore fluid chemistry | Initial pore water | Inflow water | Unit |
|------------------------|-----------------------|--------------|----------------------|
| Dissolved ions: | | | |
| Cl^- | 158.8 | 0.369 | mol/m^3 |
| SO_4^{2-} | 34.7 | 0.150 | mol/m^3 |
| HCO_3^- | 0.43 | 2.593 | mol/m^3 |
| Ca^{2+} | 22.2 | 1.00 | mol/m^3 |
| Mg^{2+} | 27.1 | 0.387 | mol/m^3 |
| Na^+ | 129.9 | 0.461 | mol/m^3 |
| K^+ | 1.10 | 0.026 | mol/m^3 |
| pH | 7.72 | 8.72 | - |
| Mineral contents: | | | |
| Anhydrite | 0 | - | mol/kg soil |
| Gypsum | 0.0054 | - | mol/kg soil |
| Halite | 0 | - | mol/kg soil |
| Calcite | 0.06 | - | mol/kg soil |
| Exchangeable contents: | | | |
| Ca-X_2 | 17.1×10^{-2} | - | mol/kg soil |
| Mg-X_2 | 16.7×10^{-2} | - | mol/kg soil |
| Na-X | 30.4×10^{-2} | - | mol/kg soil |
| K-X | 1.9×10^{-2} | - | mol/kg soil |

991

Table 3. Thermal and hydraulic properties and relationships

| Relationships | Variables | Constants |
|---|------------------------------|---|
| Thermal conductivity: | | |
| $\lambda_T = A_2 + (A_1 - A_2) \left[1 + \exp\left(\frac{S_l - x_0}{d_x}\right) \right]^{-1}$ | S_l : Degree of saturation | $A_1 = 0.52$ $A_2 = 1.28$ $x_0 = 0.65$ $d_x = 0.1$ |
| Moisture retention: | | |
| $S_l = S_{l0} + (S_{lmax} - S_{l0}) \left[1 + \left(\frac{s}{p_0}\right)^{1/(1-\alpha)} \right]^{-\alpha}$ | s : Suction (MPa) | $S_{l0} = 0.1$ $S_{lmax} = 1.0$ $p_0 = 30 \text{ MPa}$ $\alpha = 0.32$ |

992

993

Table 4. Parameters used in the hydration/dehydration model for the FEBEX bentonite in order to calculate the interlayer hydrate water content.

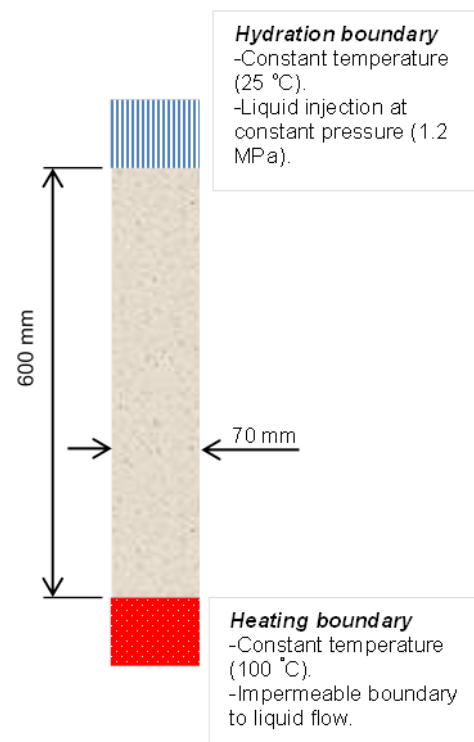
994

| Parameter | | Value |
|---------------------------------------|-------------------------------------|--|
| n_c | moles/ $\text{O}_{10}(\text{OH})_2$ | 4.5 |
| v_{il} | m^3/mole | 17.22 |
| m_{sm} | $\text{g/mol O}_{10}(\text{OH})_2$ | 376.234 |
| ρ_d^{sm} | kg/m^3 | 1580 |
| Composition/thermodynamic parameters: | | Ca-smectite Mg-smectite Na-smectite |
| Content | % | 37 34 29 |
| W_s | kcal/mol | -2883 -2806 -3254 |
| $(\log K_{eq})_{T_r}$ | $T_r = 25^\circ\text{C}$ | -3.61 -4.28 -0.767 |
| $(\Delta H_r^0)_{T_r}$ | kcal/mol | 9630 10,609 5810 |
| ΔC_p^0 | cal/mol | 69.13 |

995

996

997



998

999 **Fig.1.** Schematic of the heating and hydration experiments reported by Villar et al., (2008).

1000

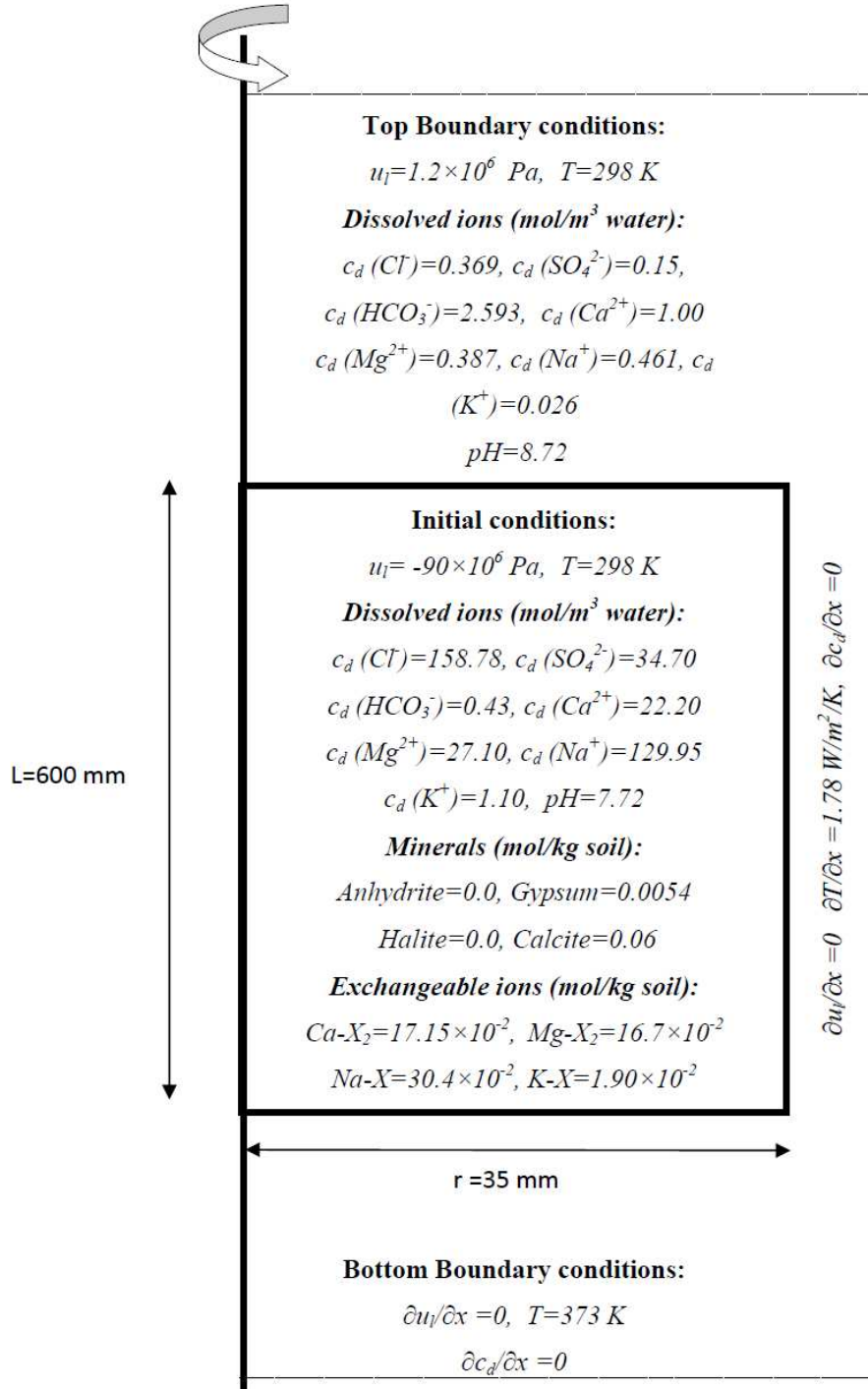


Fig.2. The initial and boundary conditions applied for coupled thermal, hydraulic and chemical simulation of the heating and hydration experiments.

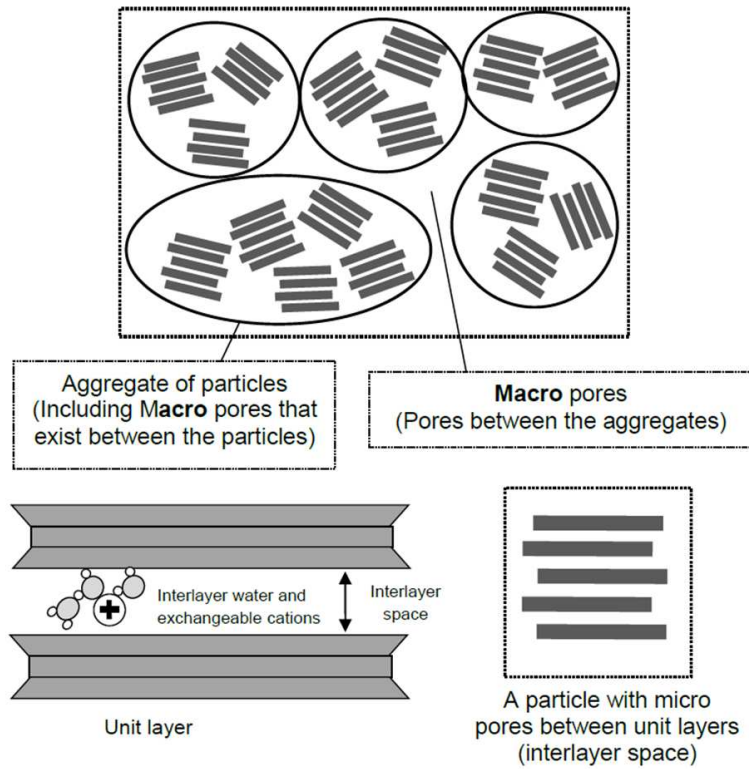


Fig.3. Schematic of the “micro porosity” and “macro porosity” definition in compacted smectite clay.

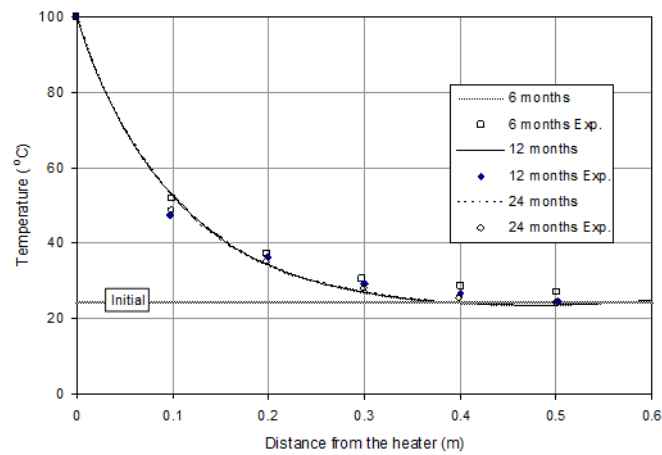


Fig.4. Variations of temperature in the domain obtained from the *transient analysis* (lines) and experiments (Villar et al., 2008b) (symbols).

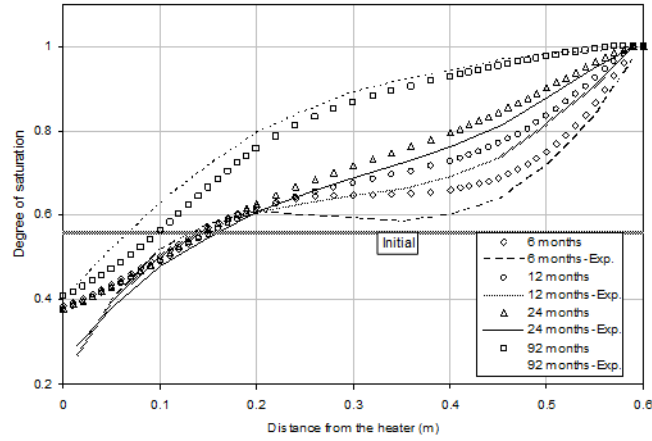


Fig.5. Variations of degree of saturation in the domain obtained from the *transient analysis* (symbols) and experiments (calculated from data by Villar et al., 2008b) (lines).

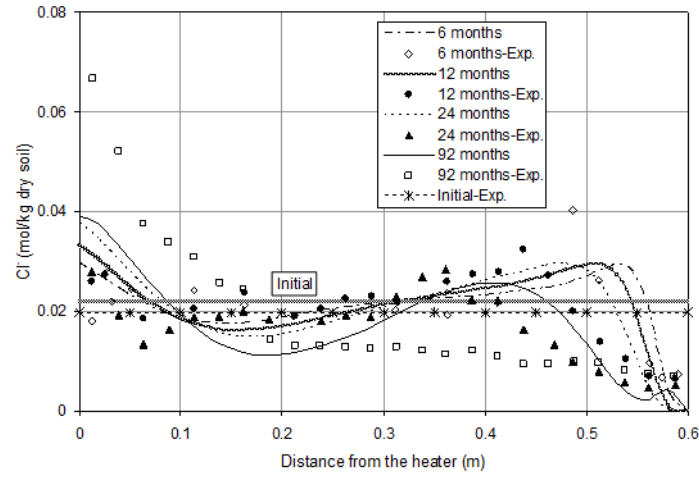


Fig. 6. Variations of chloride in the domain obtained from the *transient analysis* (lines) and experimental results (Fernández and Villar, 2010) (symbols).

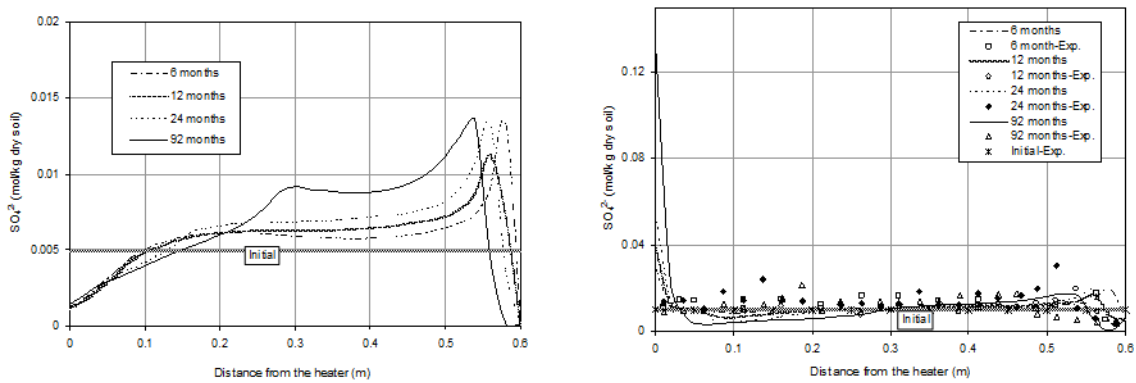


Fig. 7. Variations of sulfate in the domain obtained from the *transient analysis* (left) and *post-mortem* (right) analysis. Experimental results (symbols) are form Fernández and Villar (2010).

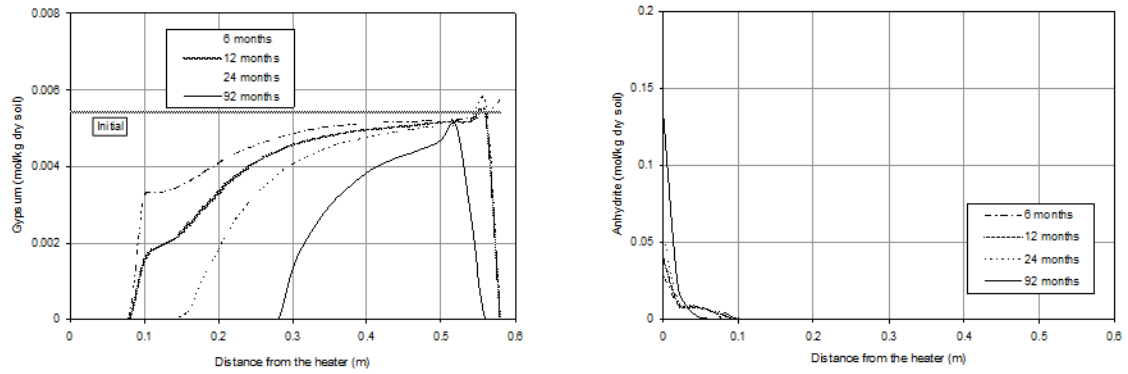


Fig.8. Variations of gypsum (left) and anhydrite (right) in the domain obtained from the *transient analysis*.

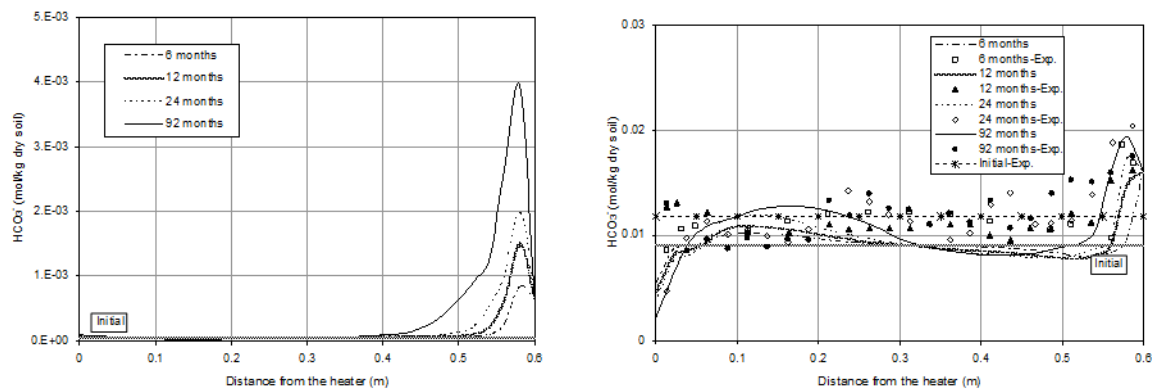


Fig.9. Variations of bicarbonate in the domain obtained from the *transient analysis* (left) and *post-mortem* (right) analysis. Experimental results (symbols) are form Fernández and Villar (2010).

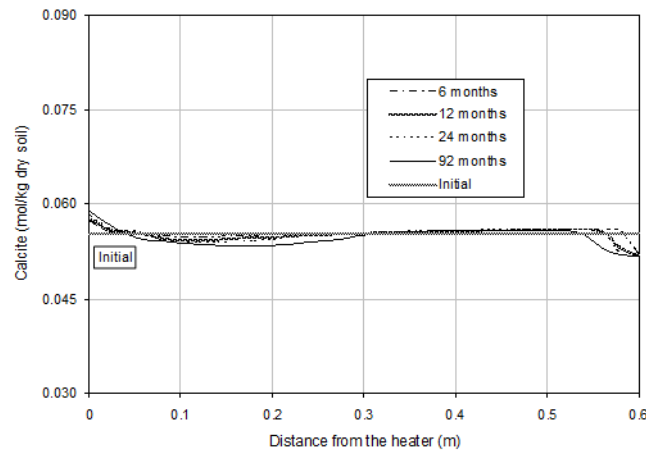


Fig.10. Variations of calcite in the domain obtained from the *transient analysis*.

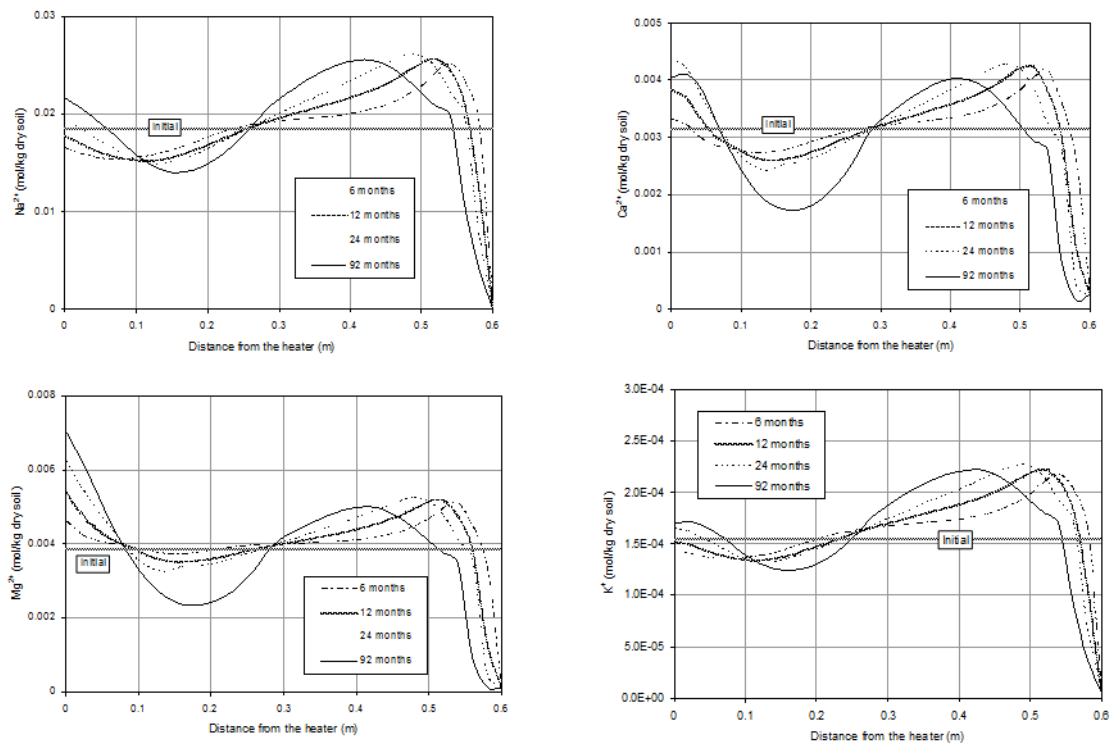


Fig.11. Variations of cationic ions in the domain obtained from the *transient analysis*.

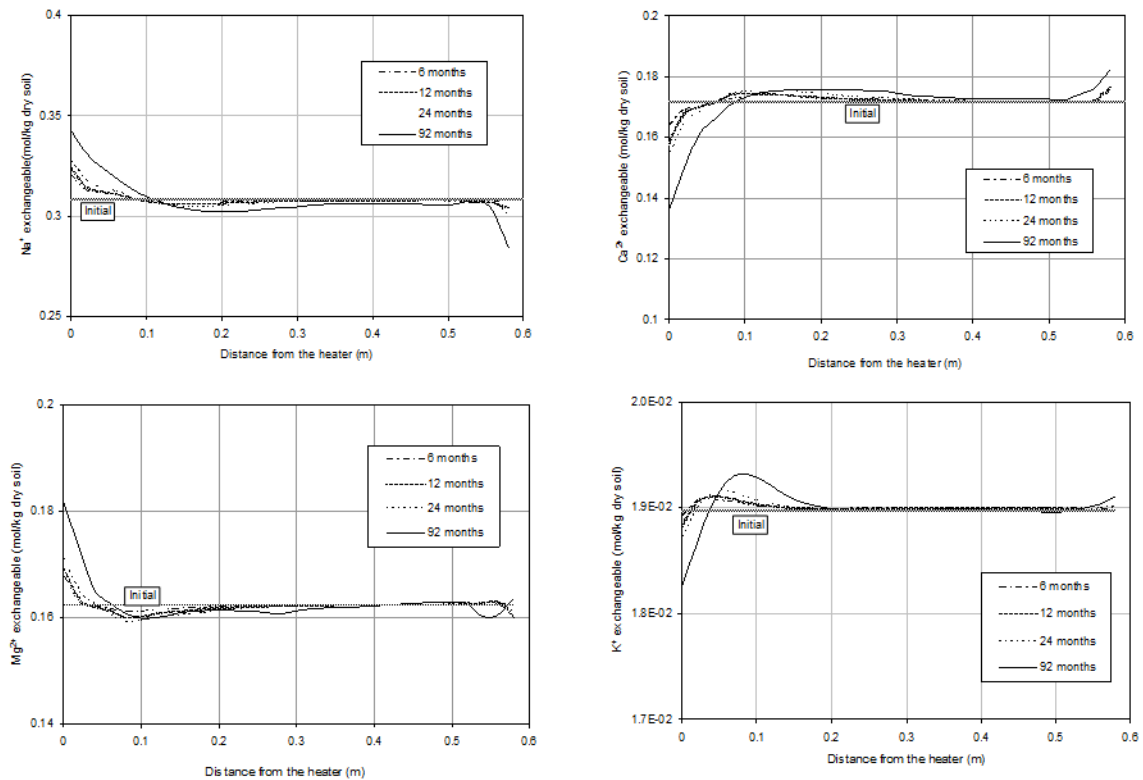


Fig.12. Variations of exchangeable ions in the domain obtained from the *transient analysis*.

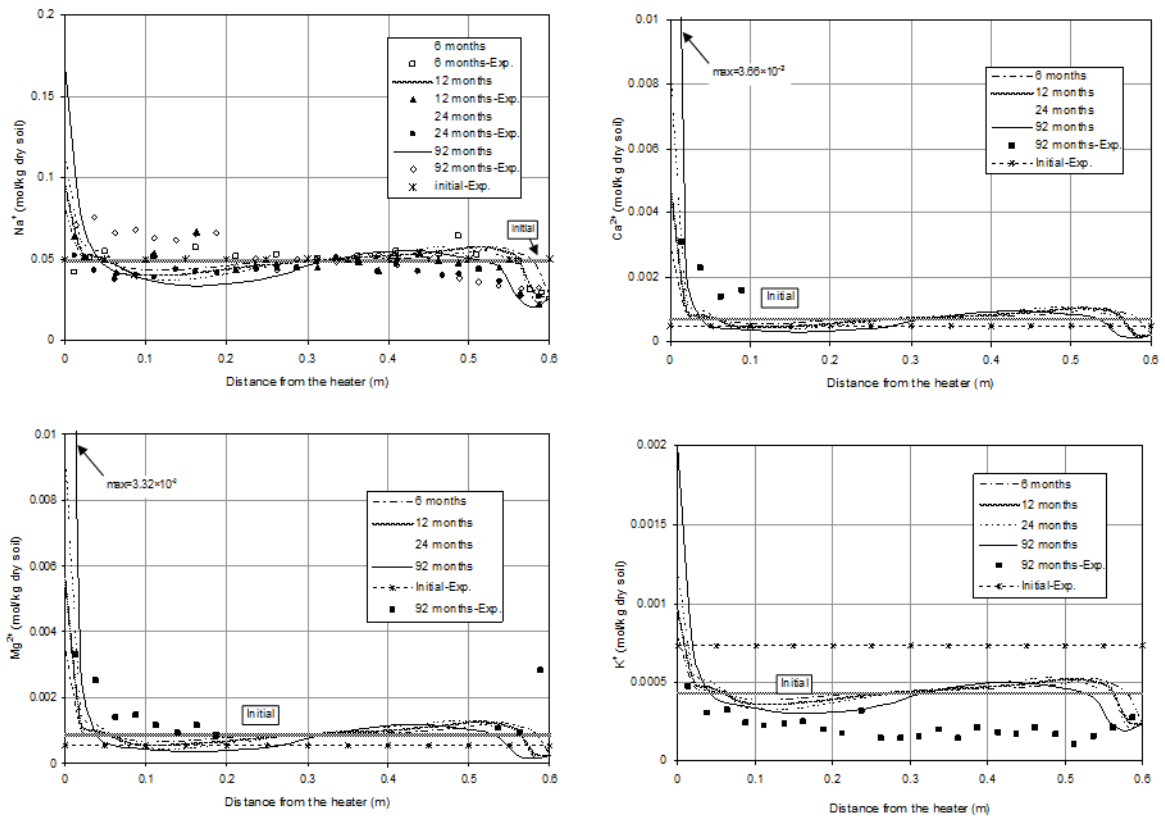


Fig.13. Variations of cationic ions in the domain obtained from the *post mortem analysis* (lines) and experiments (Fernández and Villar, 2010) (symbols).

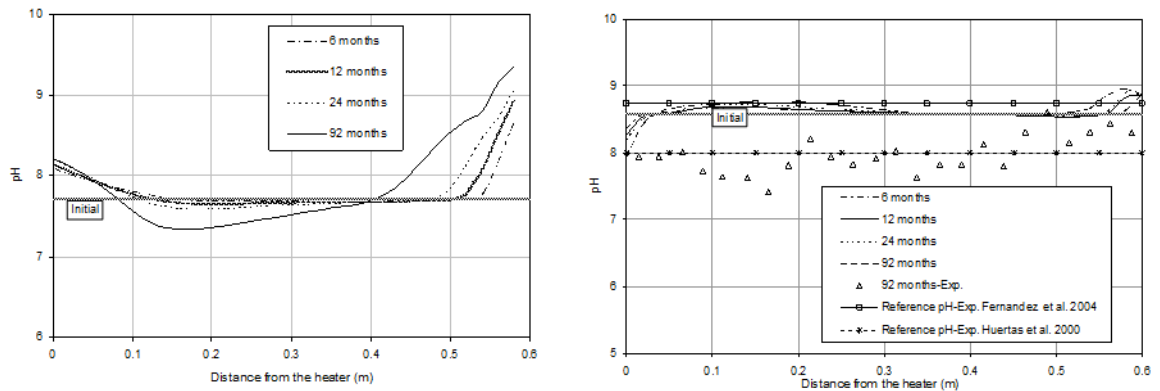


Fig.14. Variations of pH in the domain obtained from obtained i) from *transient analysis* (left) and ii) the *post mortem analysis* (left) where and experiments (Fernández and Villar, 2010) are also presented (symbols).

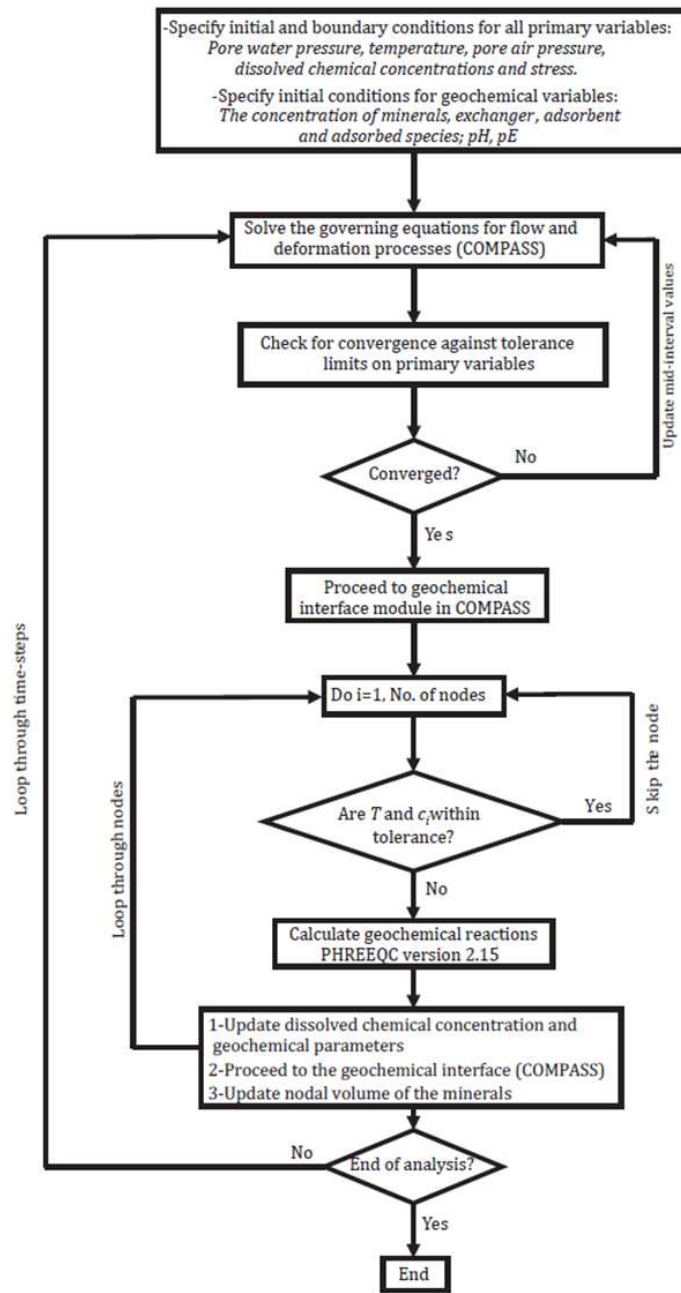


Fig.B1. The sequential non-iterative approach (SNIA) adopted for coupling the transport model (COMPASS) and geochemical model (PHREEQC).